applied sciences

MDPI

Article

Coordinated Control Method for Electromagnetic Load Reduction and Flux-Leakage Suppression in Thrust Bearings of Vertical Hydro-Generators

Lijie Hu [1,†], Jing Bai [1,†] and Jian Wu [2,*,†]

[1] Harbin Electric Machinery Company Limited, Harbin 150040, China; hulj@hec-china.com (L.H.); baij@hec-china.com (J.B.)

[2] School of Electrical Engineering and Automation, Harbin Institute of Technology, Harbin 150001, China

* Correspondence: wujianhit@hit.edu.cn; Tel.: +86-451-86413651

† These authors contributed equally to this work.

Abstract

Thrust bearings are critical load-bearing components in large vertical hydro-generators, and their operational stability directly affects unit reliability. Conventional thrust bearings face severe challenges including high friction loss, excessive pad temperature and oil-film rupture risk under heavy-load conditions. Electromagnetic load-reduction technology can share a large portion of the axial thrust load, but existing control schemes suffer from slow dynamic response, large thrust fluctuation and insufficient flux-leakage suppression under complex operating conditions. In this work, a 60 t-class vertical electromagnetic load-reduction thrust bearing test platform is designed, and a coordinated control method based on load–magnetic field–current three-loop excitation control and independent flux-leakage compensation is proposed, with oil-film monitoring and branch-output coordination implemented as auxiliary supporting modules whose independent effect was not separately validated. Experimental results show that the proposed method achieves a steady-state load regulation error below 3% over the 20–80% load-reduction range, responds smoothly to step-load changes, and suppresses the external flux leakage by over 60%; meanwhile, the measured oil-film thickness remains above the minimum safe threshold of 30 μm. This work provides experimental verification and engineering design guidance for the application of electromagnetic load-reduction technology in large hydro-generator thrust bearings.

Keywords: thrust bearing; electromagnetic load reduction; flux-leakage compensation; three-loop control; oil-film thickness; hydro-generator

Academic Editor: Alessandro Lo Schiavo

Received: 3 November 2026
Revised: 17 November 2026
Accepted: 18 November 2026
Published: 20 November 2026

Copyright: © 2026 by the authors. Licensee MDPI, Basel, Switzerland. This article is an open access article distributed under the terms and conditions of the Creative Commons Attribution (CC BY) license.

1. Introduction

In large vertical hydro-generator units, the thrust bearing carries the entire axial hydraulic thrust and rotor weight, and its operating reliability is fundamental to unit safety. As hydro-generators develop toward larger capacity and higher rotational speed, conventional thrust bearings face increasingly prominent challenges: high friction loss increases the design difficulty of the oil circulation and cooling system, excessive pad temperature raises the risk of oil-film rupture and pad burning, and unnecessary churning loss conflicts with energy-saving requirements [1,2].

Electromagnetic load-reduction technology provides a new solution for thrust bearing operation. A stationary iron core fixed to the concrete foundation and a rotating iron

core coupled to the rotor generate a controllable axial electromagnetic force that can share up to 80% of the total thrust load [3-5,, significantly reducing the load carried by the conventional thrust bearing. Research on electromagnetic actuators and magnetic bearings for rotating machinery has developed along several complementary threads. The modelling and design of active and hybrid magnetic bearings have been investigated with attention to force–current nonlinearity, magnetic saturation, eddy currents and leakage flux [6-9], while the geometric design of axial magnetic actuators and dedicated thrust actuators has been optimized for force density and low parasitic attraction [4,5,10]. Vibration suppression, unbalance compensation and rotor stability control have been addressed through observer-based balancing, synchronous-frame control, adaptive compensation and active power-amplifier regulation [11-17]. Leakage-flux modelling and structural mitigation of combined radial–axial magnetic actuators have also been reported [9,18,19], and bearing-fault diagnosis using electrical signals has been examined [20]. These studies provide a basis for electromagnetic actuation, but most are conducted at the component or simulation level and concentrate on a single control objective.

The mounting scheme of the thrust bearing, and in particular the way the bearing is axially retained, is also relevant to the friction loss and therefore belongs to the state of the art. In large vertical units the axial position of the rotor is fixed by the thrust head and the bearing bracket, and the pads are carried on a self-equalizing support mounted on spring plates or levelling jacks, so that the axial stiffness of the retaining structure, the clearance provided for differential thermal expansion and the equalization of pad load jointly determine the operating film thickness and the pad tilt. A rigid axial retention that leaves no allowance for differential expansion between the shaft and the bearing bracket reduces the film thickness as the unit heats up and thereby raises both the friction loss and the pad temperature, whereas a retention arrangement with adequate axial compliance and pad-load equalization keeps the film thickness more uniform around the annulus and the load shared among the pads. The mounting scheme thus acts on the friction loss mainly through the film thickness and the pad load distribution rather than through the friction coefficient alone. In the present work the axial position of the rotor is not fixed by a mechanical retainer: as described in Section 2.1, the 6 mm working gap of the electromagnetic actuator is the equilibrium position of the axial force balance between the oil film and the electromagnetic force, so the film thickness adjusts with the load-reduction ratio, and the axial retention of a real unit is represented only through the axial force balance that the platform reproduces.

Despite these advances, three research points remain for electromagnetic load reduction in heavy-duty thrust bearings. First, most existing control schemes rely on a single current closed loop; under the magnetic saturation and nonlinear force–current characteristics of a heavy actuator, a single loop cannot simultaneously achieve accurate load tracking, fast rejection of current and load disturbances, and small transient thrust fluctuation [6,10,17]. Second, external leakage flux shifts the effective air-gap flux density and disturbs the nearby precision sensors; although leakage-flux modelling and structural shielding have been studied [9,17], an active, independently-regulated compensation loop coordinated with the main thrust-control loop has rarely been reported. Third, oil-film operating state remains an important safety constraint, and full-scale heavy-duty experimental evidence reporting measured load regulation, leakage suppression and the corresponding oil-film state on the same platform is still lacking.

The novelty and main contributions of this paper are summarized as follows. (1) A nested load–magnetic-field–current three-loop excitation controller is proposed for heavy-duty electromagnetic actuators. This paper describes the architecture, while quantitative performance metrics are presented in Section 3. (2) Independent inner and outer

active flux-leakage compensation branches, each with its own current inner loop, cancel the external leakage flux without degrading the main thrust control. The measured leakage-suppression level is presented in Section 3. The proposed architecture is validated on a synchronized multi-sensor heavy-duty test platform, providing experimental rather than purely numerical evidence for this class of control system.

The remainder of this paper is organized as follows: Section 2 describes the 60 t-class test platform and the architecture of the proposed coordinated control method; Section 3 presents the steady-state and transient experimental results; Section 4 discusses the control performance and the limitations of the present tests; and Section 5 draws the conclusions. The proposed method provides a practical, experimentally verified control solution for electromagnetic load-reduction thrust bearings in large vertical hydro-generators and a reference architecture for related electromagnetic actuators.

2. Materials and Methods

The vertical electromagnetic load-reduction thrust bearing test platform is assembled vertically on a rigid foundation. From top to bottom, the platform consists of an electromagnetic loading system, the test thrust bearing assembly, an oil sump support frame and a drive motor frame. The drive motor transmits torque to the main shaft, reproducing the rotational speed condition of a real hydro-generator unit, while the electromagnetic loading system applies a controllable axial load that mimics the hydraulic thrust of the turbine runner. The instrumented bearing assembly enables direct measurement of oil-film thickness, pad temperature, friction loss and electromagnetic parameters under combined rotational speed and axial load.

2.1. Design of the 60 t-Class Test Platform

The test platform is designed from the control-experiment perspective as a vertical-axis hardware-in-the-loop system that reproduces the operating condition of large vertical hydro-generator thrust bearings. Its actuation part consists of the electromagnetic load-reduction unit as the controlled object, the instrumented test-bearing assembly that embodies the controlled plant state, and a variable-speed drive unit that provides a controllable rotational-speed input. The drive unit simulates the rotor rotation of an actual hydropower unit, while the electromagnetic load-reduction unit generates a continuously adjustable axial force that emulates the hydraulic thrust of the turbine runner. These units are arranged vertically on a rigid foundation so that the same axial load-transfer path as a real hydro-generator thrust bearing is reconstructed. Figure 1 summarizes the corresponding hardware-in-the-loop signal and power flow, including the host computer, dual-core DSP controller, constant-current sources, signal-conditioning chain and the 60 t test system.

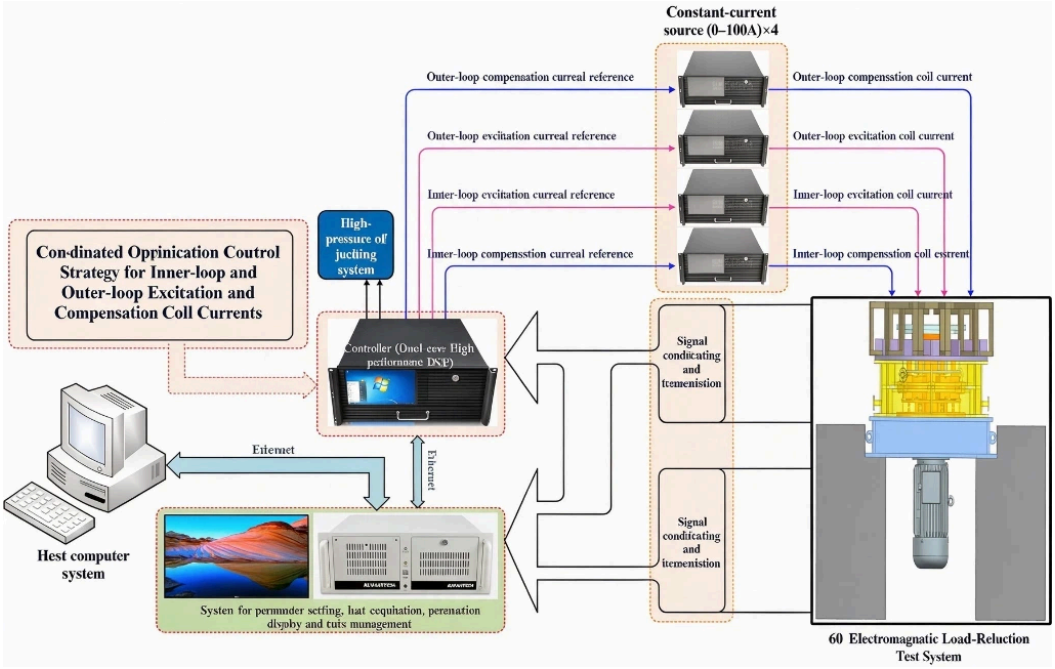


Figure 1. Overall architecture of the electromagnetic load-reduction control system (host computer, dual-core DSP controller, constant current sources, signal conditioning and the 60 t test system).

As the main controlled actuator, the electromagnetic load-reduction unit is composed of a stationary stator iron core fixed to the foundation and a rotating thrust disk coupled to the main shaft, with inner, middle and outer magnetic poles arranged concentrically. Each pole region carries independently fed excitation and compensation coils. When the excitation coils are supplied with a controlled current, an axial electromagnetic attraction force is produced between the stator and the thrust disk, which offloads a programmable fraction of the total thrust from the test bearing. The compensation coils, driven by independent current channels, generate canceling magnetic fields to suppress the leakage flux, so that the net axial force remains accurate under varying operating points and the stray magnetic field near the measurement sensors is kept within tolerance.

Directly below the electromagnetic actuator sits the instrumented test-bearing assembly, which is the physical plant whose operating state is shaped by the closed-loop control. The bearing under evaluation is fitted with dense monitoring instrumentation so that oil-film thickness, pad temperature, oil-cavity pressure and friction loss can be sampled simultaneously under combined speed and axial-load conditions. A lubrication circuit supplies the oil bath, and a variable-speed drive transmits torque to the main shaft through the bearing, so that any combination of rotational speed and offload ratio can be established for the control experiments.

The hydrodynamic oil film between the rotating runner and the stationary pads is the fundamental controlled quantity of the bearing. Sector-shaped babbitt-lined pads are distributed around the annular bearing seat and support the mirror plate rigidly mounted on the main shaft; under rotation, a thin lubricating film builds up between the two surfaces and carries the axial load. The film thickness thus reflects the instantaneous supporting state and thermal margin of the bearing. PT100 sensors embedded in the pads and eddy-current displacement sensors arranged along the circumference provide pad-temperature and film-thickness signals in real time, which are used by the closed-loop controller and the auxiliary signal channel described in Section 2.2.

Guide pads arranged around the main shaft constrain radial vibration and keep the rotor within the allowable clearance, so that the electromagnetic actuator operates around a well-defined nominal position. In the magnetic circuit, the working air gap between the stationary stator and the rotating thrust disk is the key state variable that links the coil current to the produced axial force through Equation (1); its nominal value is 6 mm in this device. The guide pads constrain only the radial position of the main shaft and provide no axial positioning, so the 6 mm value is not enforced by the guide-bearing system; it is the equilibrium gap of the axial force balance between the hydrodynamic oil film of the thrust bearing and the electromagnetic force of the actuator. With the thrust pads, oil film, air gap and loading disk working together, the platform reproduces the load-transfer chain of a real vertical hydro-generator thrust bearing and provides a physical test bench on which the coordinated control strategy can be validated under repeatable conditions.

The magnetic thrust generation principle of the electromagnetic load-reduction device can be analyzed by the magnetic circuit method. The flux path begins at the stator yoke, crosses the working air gap, enters the rotating thrust disk, and returns through the second air gap and the pole body. The iron core is divided into compensation, excitation and outer compensation regions. The nominal working air-gap at the equilibrium position determines the operating flux density through Equation (1), and therefore directly controls the attainable electromagnetic force given by Equation (2). Equations (1) and (2) connect the air-gap geometry, coil excitation and output thrust force, providing the physical basis for the proposed feedback-oriented multi-loop controller.

$$B = \mu_0 \cdot NI/(2\delta) \quad (1)$$

$$F = B^2 \cdot S/\mu_0 \quad (2)$$

where NI is the magnetomotive force, μ0 is the permeability of air, δ is the single-side working air gap, and S is the effective pole area. At the maximum excitation current of 55 A, the maximum load capacity obtained from the finite-element field solution reaches approximately 641 kN, which meets the design target of 60 t.

Equations (1) and (2) constitute an ideal double-gap magnetic-circuit model and are used only for preliminary dimensioning and for providing the initial parameters of the inverse model of the excitation loops. The model assumes two identical air gaps and a uniform air-gap flux density, and neglects the fringing flux at the pole edges, the leakage flux outside the working gap and the reluctance of the iron core. In Equation (2), the effective pole area S is the sum of the annular areas of the three concentric excitation pole rings, as expressed in Equation (3).

$$S = \Sigma_{i=1,2,3} (\pi/4)(D_{out,i}^2 - D_{in,i}^2) \quad (3)$$

where i = 1, 2 and 3 denote the inner, middle and outer excitation pole ring, respectively, and $D_{out,i}$ and $D_{in,i}$ are the outer and inner diameters of ring i. The inner, middle and outer rings have inner/outer diameters of 800/1020 mm, 1164/1468 mm and 1612/1732 mm, respectively, which gives a total effective pole area of $S \approx 1.26\ m^2$. The compensation pole rings are not included in S, because their flux is commanded to cancel the external leakage flux and does not contribute to the net axial force.

These simplifications are acceptable at the sizing stage because Equation (2) is not used to produce the reported capacity: the value of approximately 641 kN at 55 A and a 6 mm single-side gap is obtained from the finite-element field solution of the actuator, in which the actual pole geometry, the fringing flux at the pole edges and the leakage paths outside the working gap are represented explicitly and the nonlinear B–H characteristic

of Q355B is included, so that iron saturation is accounted for. The magnetic-circuit equations therefore fix the initial dimensions and initialize the controller, whereas the field solution supplies the load capacity; the force applied in operation is generated from the pre-calibrated nonlinear B–I and F–I characteristics described in Section 2.2.2 and corrected by the closed force loop. It is worth noting that, for this pole area, the reported capacity corresponds to an equivalent average working-gap flux density of about 0.80 T at 55 A, which lies in the linear range of the Q355B core and is consistent with the flux densities obtained from the field solution. The mesh-independence check for this field solution is summarized in Table 1.

Table 1. Mesh-independence check of the 2D transient finite-element model at 55 A and a 6 mm single-side working gap.

Mesh	Gap-Region Elements	Total Elements	Axial Force/kN	Relative Error vs. Fine Mesh
Coarse	~0.3k	~1.7k	636.791	0.7280%
Medium 1	~5.9k	12.1k	640.703	0.1185%
Medium 2	~12.4k	23.2k	641.213	0.0390%
Fine (reference)	~21.8k	43.6k	641.463	—

Because the ANSYS Maxwell 2D transient solver does not perform adaptive mesh refinement, the discretization quality was verified manually by solving the model on four meshes, with local refinement of the air-gap region in the medium and fine cases (Table 1). The adopted medium-2 mesh yields an axial force of 641.213 kN, only 0.039% below the fine reference value of 641.463 kN, whereas the coarse mesh deviates by 0.7280%. The reported capacity has therefore converged with respect to the finite-element discretization.

The platform is equipped with a synchronized multi-channel measurement chain: a capacitive non-contact displacement sensor measures the working air gap between the actuating disk and the force-receiving disk, eddy-current displacement sensors measure the oil-film thickness, PT100 probes monitor pad, oil-bath and coil temperatures, current transformers (CTs) sample the excitation and compensation coil currents, flux-density probes detect the main-pole and stray-leakage flux, and pressure transducers record the oil-cavity pressure. After conditioning, all analog signals are sampled synchronously by the lower DSP controller and the upper industrial computer, supplying the complete state vector required by the multi-loop coordinated control law in Section 2.2. Figure 2 gives workshop photographs of the assembled mechanical test platform and the electromagnetic load-reduction control cabinets.









Figure 2. Photographs of the 60 t-class electromagnetic load-reduction thrust bearing test platform in the workshop and the control cabinets of the electromagnetic load-reduction system.

The eddy-current displacement sensors used to measure the oil-film thickness were calibrated against reference standards before the test campaign. Their measuring range is 0–2000 μm, with a declared comprehensive accuracy of 0.5% of full scale. The capacitive sensor that measures the working air gap between the actuating and force-receiving disks is a commercial instrument whose specifications are listed in Table 2. The 30 μm minimum safe threshold is an empirical engineering criterion for this babbitt-lined thrust-pad bearing, derived from equipment design and field-operation experience rather than from sensor calibration; when judging whether the operating oil film meets the safety requirement, the measurement accuracy of the sensors is taken into account together with this empirical threshold.

Table 2. Controller parameters and measurement-channel characteristics.

Parameter	Value	Basis
Control and sampling period	1 ms	synchronous multi-channel acquisition
Load-loop PI gains	K_{pL} = 0.01, K_{iL} = 0.005	tuned last, lowest bandwidth
Magnetic-field-loop PI gains	K_{pB} = 0.01, K_{iB} = 0.005	B–I lookup as forward model
Current-loop PI gains	K_{pi} = 0.1, K_{ii} = 0.05	tuned first, highest bandwidth
Excitation current limit	55 A	actuator maximum
Working air gap (actuating disk to force-receiving disk)	3–15 mm, ±3% FS	CS15 capacitive non-contact displacement sensor (Chengdu Gaoshen Technology, Chengdu, China), 4–20 mA output; manufacturer certificate
Oil-film thickness	0–2000 μm, 0.5% FS (±10 μm)	Bently-Nevada eddy-current sensor, probe 330903-00-08-70-02-00, proximitor 330980-71-00 (Bently Nevada, Minden, NV, USA); calibrated against reference standards
Temperature channels (thrust pad, oil bath, coil)	0–100 °C, Class B (IEC 60751), ±(0.30 + 0.005|t|) °C	PT100 (Heraeus, Hanau, Germany), manufacturer certificate
Excitation and compensation current channels	0–100 A, ±0.5% FS	current transformer (CT) (Shanghai Acrel, Shanghai, China), manufacturer certificate
Main-pole flux-density channel (HGA-2010, transverse-mounted)	0–2 T (0–20,000 Gs), 1 mA constant-current excitation; probe sensitivity 11–28 mV/kGs; system-level accuracy ±1.5% FS	HGA-2010 transverse Hall probe with self-developed transmitter; in-house system-level calibration (the probe vendor specifies sensitivity only, without a standalone full-scale accuracy)
Leakage-flux-density channels (inner and outer)	0–1000 Gs (0–100 mT), non-linearity ±1% FS	TMR2151S TMR sensor (Toshiba, Tokyo, Japan), manufacturer certificate
Oil-cavity pressure channel	0–40 MPa, ±0.1% FS BSL	PTX5062-TD-A2-CA-H0-PN (Druck, Leicester, UK), manufacturer certificate

The bearing mounting of the real vertical hydro-generator unit and of the test platform is compared in Figure 3, so that the constructive similarities and differences between the real case and the test rig can be identified directly.

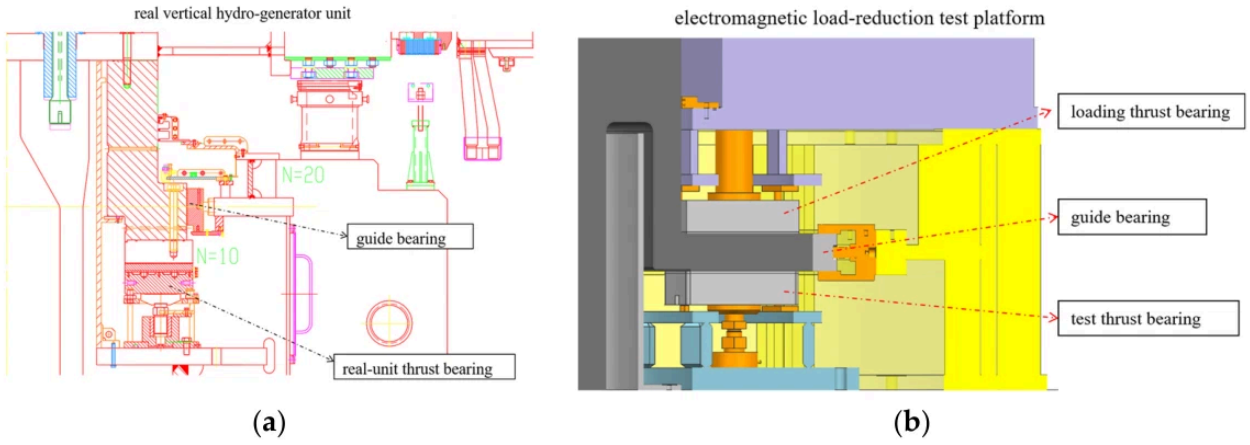


Figure 3. Sectional comparison of the bearing mounting: (**a**) real vertical hydro-generator unit; (**b**) electromagnetic load-reduction test platform.

In the real hydro-generator unit, the oil sump contains only two bearings: the thrust bearing and the guide bearing. The thrust load on the bearing is supplied by the weight of the rotating assembly together with the hydraulic thrust acting on the turbine runner.

In contrast, the oil sump of the test platform contains three bearings: the test thrust bearing, the guide bearing, and an additional loading thrust bearing. The thrust load applied to the test thrust bearing is imposed by this loading thrust bearing, which reproduces the hydraulic thrust of the real unit.

The two configurations share the vertical arrangement, the babbitt-lined tilting-pad thrust bearing and the guide bearing, and the same hydrodynamic lubrication principle. The main constructive difference is that the test rig introduces the extra loading thrust bearing, which allows the thrust load to be adjusted flexibly and independently, so that the electromagnetic load-reduction behavior can be investigated under different thrust-load conditions.

The actuator adopts a concentric multi-pole ring layout with inner, middle and outer magnetic poles along the radial direction. The stationary stator is anchored to the test foundation, while the rotating thrust disk of 1738 mm outer diameter follows the main shaft, leaving a single-side working air gap of 6 mm. Both stator and rotor magnetic-conducting parts are fabricated from Q355B steel, and the coil conductors are made of copper, so that the actuator exhibits a predictable magnetic behavior suitable for feedback-linearizing control design.

The excitation coils adopt 200 turns and the compensation coils adopt 100 turns. The maximum excitation current is 55 A with a maximum voltage of 58 V, and the maximum compensation current is 50 A. The current density of the excitation coils is 2.5 A/mm^2 at the rated excitation, and the air-gap flux densities of the inner, middle and outer poles reach 1.085 T, 1.144 T and 1.084 T, respectively. The DC losses of the inner and outer excitation coils at 120 °C are 2260.3 W and 3187.6 W, respectively.

The characteristic is nearly linear at low current and rolls off gradually as the iron approaches magnetic saturation; this mild nonlinearity is explicitly accounted for by the multi-loop control structure of Section 2.2.

Under heavy-load operating conditions, the actuator suffers from magnetic saturation and nonlinear force-current behavior; hence, the multi-loop control strategy described in Section 2.2 is required to maintain load-tracking accuracy and suppress transient thrust fluctuation.

Test Program

The test program was defined to reproduce the operating conditions of a real vertical hydro-generator thrust bearing on the 60 t-class platform. The controlled input parameters are the rotational speed and the load-reduction ratio. The rotational speed is held at 500 r/min, the rated speed of the driving motor on this platform; the load-reduction ratio is commanded by the load loop and denotes the fraction of the total axial thrust shared by the electromagnetic actuator. The steady-state cases were selected at load-reduction ratios of 0%, 20%, 40%, 60% and 80%, following the bearing performance calculation cases used in the design of the real-unit thrust bearing; the same type of lubricant used in large vertical hydro-generator thrust bearings was employed, and the inlet oil temperature was set to the design value of the real bearing. In addition to the steady-state cases, stepwise loading and load-reduction ramps between these ratios were recorded as transient cases, together with the actuator-failure scenario used to verify the protection logic.

The measured output parameters are the load-reduction weight, the inner-loop and outer-loop excitation and compensation currents, the main-shaft swing in two orthogo-

nal directions, the working air gap, the main-pole flux density, the inner-loop and outer-loop leakage-flux density, the oil-film thickness, the oil-cavity pressure, and the pad, oil-film, coil and guide-pad temperatures; the oil flow and oil temperature of the external circulation loop are also monitored.

With respect to the real functioning situation, the platform retains the vertical arrangement, the babbitt-lined sector pads, the rotating runner and the hydrodynamic oil film of the real thrust bearing, so that the load-transfer chain from the axial thrust to the oil-film force and the electromagnetic force is reproduced. The hydraulic thrust of the real unit is replaced on the platform by the hydraulic loading cylinder, which applies the rated thrust, while the electromagnetic actuator provides the load-reduction force; the radial location of the shaft is still constrained by guide pads. The structural similarities and differences between the real unit and the test platform are discussed in the comparison of the mounting schemes.

Before the formal measurements, the bearing was given a running-in period: the platform was brought up to the operating speed and loaded stepwise at low load, and the formal steady-state and transient recordings were started only after the oil-film thickness, the pad temperature and the oil-cavity pressure had stabilized. In each steady-state case the platform was held at the target load until the monitored quantities were stable, so that the recorded values represent a thermally stabilised operating condition rather than a warm-up transient; in the transient cases the signals were recorded continuously along the loading or load-reduction ramp. The present test campaign covers the steady-state ratios listed above and the corresponding stepwise ramps.

2.2. Coordinated Control Method for Load Reduction and Flux Leakage Suppression

The proposed coordinated control method aims to realize high-precision thrust load regulation under complex operating conditions of the electromagnetic load-reduction test platform. The complete control workflow includes multi-source state signal acquisition, the nested three-loop excitation main control, and the independent flux-leakage compensation sub-module; auxiliary oil-film signal-based reference and branch-output coordination functions are described for implementation completeness, but were not separately validated as independent contributions. The overall architecture of the control system is illustrated in Figure 1.

2.2.1. Multi-Source State Signal Acquisition

Before executing the control calculation, the system synchronously acquires multi-dimensional state feedback signals from the test platform. The measured variables include the target and actual bearing load, the total applied load, the thrust-pad load, the oil-film thickness, the main-pole flux density, the leakage-flux density, the excitation current and the compensation current. These measured quantities provide the full-state foundation for all subsequent closed-loop regulation and avoid control deviation caused by incomplete system perception.

2.2.2. Load–Magnetic Field–Current Three-Loop Excitation Control

The three-loop control structure is nested from outside to inside as load closed loop, magnetic field closed loop and current closed loop. The outermost load loop takes the deviation between the given bearing load and the measured load, processes it through error dead zone, load regulator and output amplitude limiting, and outputs the main pole magnetic flux density setpoint. The middle magnetic field loop compares the given flux density with the measured main pole flux density, adjusts the deviation and outputs the excitation current setpoint. The innermost current loop tracks the excitation current

setpoint at high speed, drives the excitation constant current source, and rapidly suppresses current disturbances, as illustrated in Figure 4.

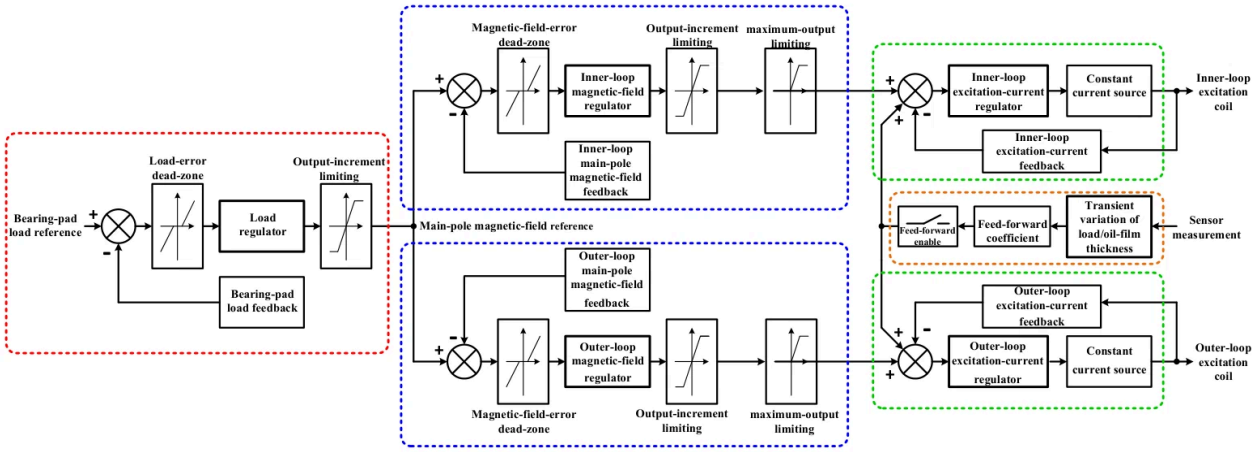


Figure 4. Three-loop excitation control block diagram of the electromagnetic load-reduction device (load–magnetic field–current nested structure with inner and outer excitation branches and auxiliary feedforward reference channel).

The inner and outer excitation branches are independently controlled: each branch is equipped with its own magnetic field loop and current loop, driving the corresponding inner and outer excitation coils, thus realizing independent regulation of the magnetic field in different radial regions and fine adjustment of the thrust distribution.

The load regulator and the inner/outer main-pole magnetic-field regulators combine pre-calibrated nonlinear B–I and electromagnetic-force F–I lookup relations with recursive discrete-time PI regulation. The inner and outer excitation-current controllers are conventional PI current regulators that rapidly track the excitation-current setpoints. All controller parameters are tuned by trial-and-error on the 60 t-class platform rather than by analytical theoretical derivation; the calibrated lookup data convert load and flux-density requirements into current references. Because this paper focuses on system-level experimental validation rather than controller synthesis, detailed transfer functions and parameter-derivation equations are not presented; Figure 4 records the implemented signal architecture.

The flux-density setpoint issued by the load loop is common to the inner, middle and outer excitation rings, and it is not divided into separate inner and outer flux-density commands. The split between the inner and outer excitation-current references is produced inside the magnetic-field loop: each branch converts the common flux-density setpoint into its own current reference through the pre-calibrated inverse B–I characteristic of that ring, with Equation (1) used only as the initial estimate. The two branches therefore settle at different currents for the same flux-density command, because the rings differ in pole area, in mean flux-path length and in magnetization characteristic. The split is thus fixed by the magnetics of the actuator rather than by a manually tuned current ratio, and the force contributed by each ring is proportional to its pole area. This keeps the resultant axial force centred on the shaft axis and avoids a tilting moment between the stator and the thrust disk. The behavior is visible in the measurements in Section 3: at the same flux-density command the inner and outer branches operate at different currents, while the main-pole flux density follows the common setpoint . This distribution is part of the three-loop structure itself, and it is distinct from the auxiliary branch-output coordination logic described in Section 2.2.5.

It should be noted that the PI regulators and the pre-calibrated nonlinear B–I/F–I

lookup tables are basic building blocks of the proposed architecture; the methodological novelty does not lie in introducing new PI control elements, but in the hierarchical nested three-loop framework purposely tailored to the magnetic-saturation nonlinearity of heavy-duty electromagnetic thrust actuators, combined with the independent inner–outer leakage-flux compensation branches.

From the viewpoint of disturbance rejection, the three loops handle control objectives in different frequency bands. The innermost current loop suppresses fast high-frequency current disturbances. The intermediate magnetic-field loop compensates the nonlinear B–I characteristic caused by iron saturation through the pre-calibrated lookup data, so that this nonlinearity is not passed entirely to the outer load loop. The outermost load loop achieves low-frequency accurate thrust-load tracking. Under strong magnetic saturation, a single current loop cannot decouple these multi-band objectives simultaneously, which motivates the nested multi-loop arrangement.

The lookup tables are not ad hoc empirical tuning parameters; they represent the pre-identified nonlinear magnetic forward model of the actuator and provide the nonlinear compensation basis for the magnetic-field loop. A rigorous closed-form stability proof for this multi-input nonlinear closed-loop system is involved and remains a subject of future work; the present paper focuses on system-level experimental validation of the proposed coordinated architecture on the 60 t-class heavy-duty test platform.

2.2.3. Auxiliary Oil-Film-Thickness Signal Channel

Oil-film thickness signals reflect the transient support state of the thrust bearing. This auxiliary channel extracts the change rate of oil-film thickness and generates a reference adjustment term that can be superimposed onto the magnetic-field or current loop; its gain and enable state are configurable. The present experiments do not isolate the independent effect of this channel.

2.2.4. Independent Flux-Leakage Compensation Sub-Module

Independent inner-outer flux-leakage compensation branches are designed. Each branch collects the external leakage flux density signal, takes zero leakage flux as the control target, and generates the compensation current setpoint through the nonlinear B–I relationships calibrated by electromagnetic field simulation or experiments. The compensation current is output in the opposite direction to the excitation current, generating a reverse magnetic field to cancel the leakage flux. The inner and outer compensation-current controllers are conventional PI current regulators, whereas the inner and outer leakage-flux controllers combine the pre-calibrated nonlinear B–I lookup relations with recursive discrete-time PI regulation, as illustrated in Figure 5.

For these leakage-flux compensation branches, the inner and outer compensation-current controllers use conventional PI regulation for fast current tracking, while the inner and outer leakage-flux controllers use recursive discrete-time PI regulation based on the pre-calibrated nonlinear B–I lookup relations. The calibrated data are used directly in the controller lookup logic; because this section describes the implemented hardware/control scheme and measured suppression result rather than a closed-form regulator design, a separate analytical compensation equation and compensation-regulator transfer function are not expanded.

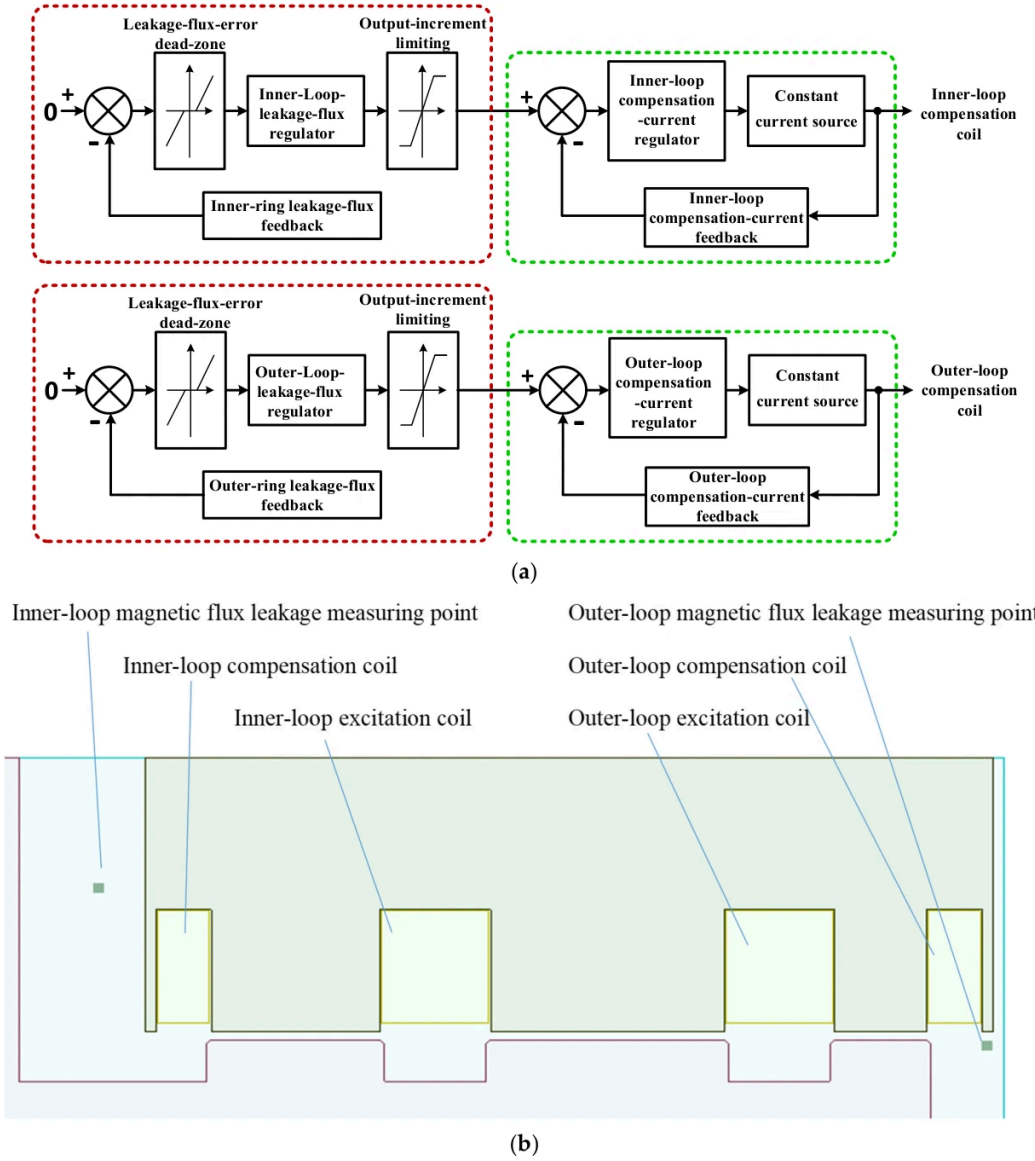


Figure 5. (**a**) Flux-leakage compensation control block diagram (independent inner-outer compensation branches with leakage-flux outer-loop and current inner-loop dual closed-loop structure). (**b**) Positions of the leakage-flux probes in the axisymmetric field model of the actuator: the inner-loop probe is at a radial distance of 30 mm from the stator bore surface at one half of the stator axial height, and the outer-loop probe is at the centre radius of the outer pole, 10 mm below the pole face.

The leakage-flux probes are not placed at arbitrary positions. As shown in Figure 5 b, the inner-loop probe is located in the bore-side air region at a radial distance of 30 mm from the stator bore surface, at one half of the stator axial height, and the outer-loop probe is located at the centre radius of the outer pole, 10 mm below the lower face of that pole, in the air region on the outer-diameter side. Both positions lie in air outside the iron, where the external leakage flux leaves the actuator on the bore side and on the outer-diameter side, namely on the two leakage paths that the inner and outer compensation branches are designed to cancel. Nulling the flux density at these two positions therefore acts on the dominant leakage exits rather than on a convenient local spot. Both the leakage field and the compensation field are axisymmetric about the shaft axis, because the poles, the working gap and the compensation coils are annular and circumferentially continuous. A leakage flux density measured at one azimuthal position therefore

represents the whole annular path at that radius, and cancelling it at the measuring position cancels it along the corresponding circumference instead of only at the sensor. The reported suppression is consequently a reduction of the external leakage flux on the bore side and on the outer-diameter side, and it is stated in these terms: residual local deviations caused by manufacturing eccentricity and by the discrete coil winding are not driven to zero and are not claimed as zero. The suppression ratio is evaluated at both probes and along the whole load-reduction ramp, so that the statement does not rest on a single operating point.

The baseline for the reported suppression is defined explicitly. The uncompensated dataset is acquired with both inner-loop and outer-loop compensation branches switched off while the excitation branches operate normally along the same load-reduction ramp; the leakage-flux density recorded in this state is the reference for every suppression value quoted. The suppression ratio is evaluated over the load-reduction range of 20% to 80%, and the same range applies to the two probes of Figure 5b. Below a load-reduction ratio of 20% the absolute external leakage-flux density is small, so a ratio referred to that level is numerically uninformative and is not quoted; no suppression value in this paper is an extrapolation outside the tested range.

2.2.5. Auxiliary Branch Output Coordination Logic

During load changes, the system calculates the required electromagnetic force according to the deviation between the total applied load and the actual test bearing load. The auxiliary coordination logic arbitrates the commands issued to the excitation and compensation branches, namely ramp-rate limiting, amplitude limiting and switching sequence, but it does not determine the split of the inner and outer excitation-current references, which is produced by the common flux-density setpoint and the per-ring inverse B–I conversion described in Section 2.2.2. Its separate effect on load-reduction ratio accuracy and thrust balance was not isolated in the present experiments.

These modules operate in a coordinated chain: multi-source state acquisition supplies real-time feedback to the main three-loop controller; the independent leakage-compensation branches run in parallel with the excitation loops. The auxiliary oil-film signal channel and branch coordination logic reconcile implementation-level signals and commands, but they are not treated as independently validated contributions in this paper.

2.2.6. Controller Implementation, Parameter Tuning and Measurement Uncertainty

The three-loop control law, the branch coordination logic and the lookup tables are implemented in the lower DSP controller, while the upper industrial computer performs supervision, data logging and operator interface functions. All analog channels described in Section 2.1 are conditioned and sampled synchronously within one and the same control cycle, so that the load, flux-density, current and displacement signals entering the three loops refer to the same time instant; this synchronous acquisition is what allows the nested loops to act on a consistent state vector instead of on channels delayed with respect to each other. The control period and the sampling period coincide, and the PI regulators are executed in recursive discrete-time form at that period, so that the implementation corresponds exactly to the discrete-time structure presented in Section 2.2.2.

The gains were tuned loop by loop, from the inner to the outer loop, and at each step the remaining loops were kept closed. The current loop is tuned first, until the current step response reaches the shortest rise time compatible with a small overshoot, because this loop carries the fastest dynamics of the chain. The magnetic-field loop is then tuned with the pre-calibrated B–I relation acting as the forward model, so that its PI reg-

ulator only compensates the residual error of that model instead of the whole magnetic nonlinearity. The load loop is tuned last and is given the lowest bandwidth of the three, so that its action on the thrust load does not interact with the two inner loops. The output of every regulator is limited, the excitation current is capped at the 55 A maximum of the actuator, and an integral anti-windup action prevents the integral term from accumulating while the output is saturated. The numerical values obtained in this way, together with the characteristics of the measurement channels, are collected in Table 2.

The measurement uncertainty is handled in the same framework. The eddy-current channel that measures the oil-film thickness has a range of 0–2000 μm and a declared comprehensive accuracy of 0.5% of full scale, which amounts to 10 μm over that range, and it was calibrated against reference standards before the campaign. The declared ranges of the remaining channels, including the capacitive channel used for the working air gap between the actuating and the force-receiving disk, are those of the commercial instruments of the measurement chain and are listed in Table 2, while their declared accuracies are those stated in the manufacturers' calibration certificates; rather than being quoted separately for each curve, they are propagated into the peak-to-peak bands reported in Section 3.7, so that every quantitative statement of the paper carries its measurement band and the conclusions are bounded by the accuracy of the chain that produced them. The main-pole flux-density channel uses an HGA-2010 Hall sensor mounted in the transverse configuration and driven by a 1 mA constant-current source; the manufacturer specifies this sensor through its factory-calibrated sensitivity of 11–28 mV/kGs only and does not state a standalone full-scale accuracy for the probe. The channel as a whole, that is the probe together with the self-developed transducer, was therefore calibrated in house, and its system-level accuracy is ±1.5% FS over the 0–2 T range.

3. Results

The test was carried out on the 60 t-class vertical test platform. The drive motor was set to the rated operating speed, and the load-reduction ratio was adjusted stepwise from 0% to 80%. The steady-state and transient waveforms of the key operating parameters were recorded by the multi-source acquisition system. The main experimental results are analyzed as follows.

3.1. Load-Reduction Weight and Excitation Current Response

Figures 6–10 show the steady-state waveforms of the reduced load weight, the inner-loop and outer-loop excitation currents and the inner-loop and outer-loop compensation currents under different load-reduction ratios. When the load-reduction ratio setpoint is varied from 0% to 80%, the actual load-reduction weight tracks the setpoint accurately, and the excitation currents change smoothly without obvious oscillation. The compensation currents respond accordingly to maintain the flux leakage suppression effect. The results indicate that the three-loop excitation control structure achieves high-precision steady-state load regulation, with a steady-state error below 3% over the 20–80% load-reduction range.

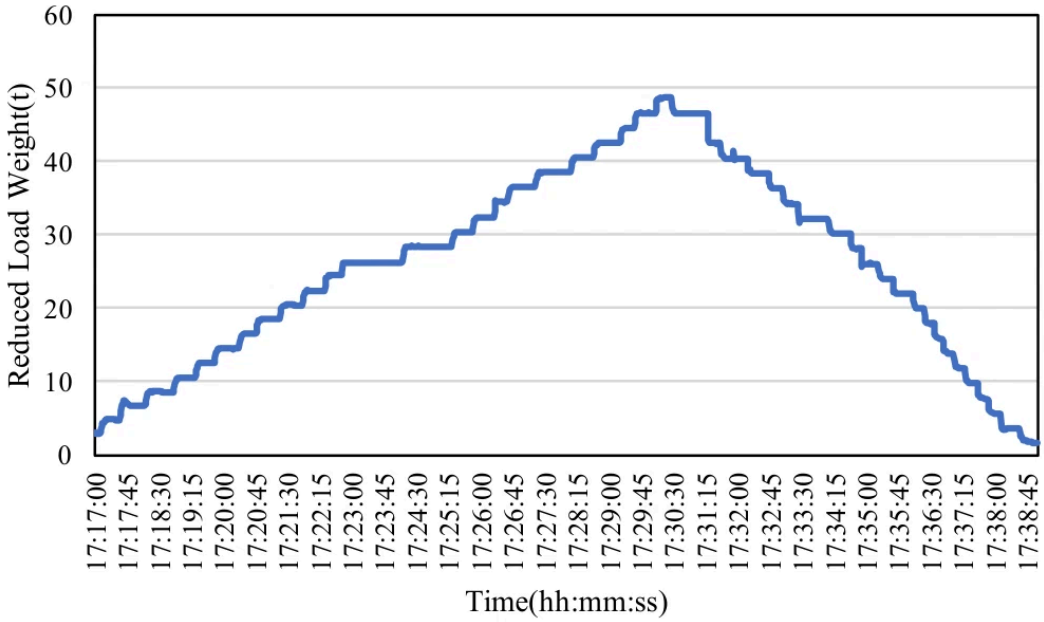


Figure 6. Load-reduction weight waveform of the test platform during the load-reduction process.

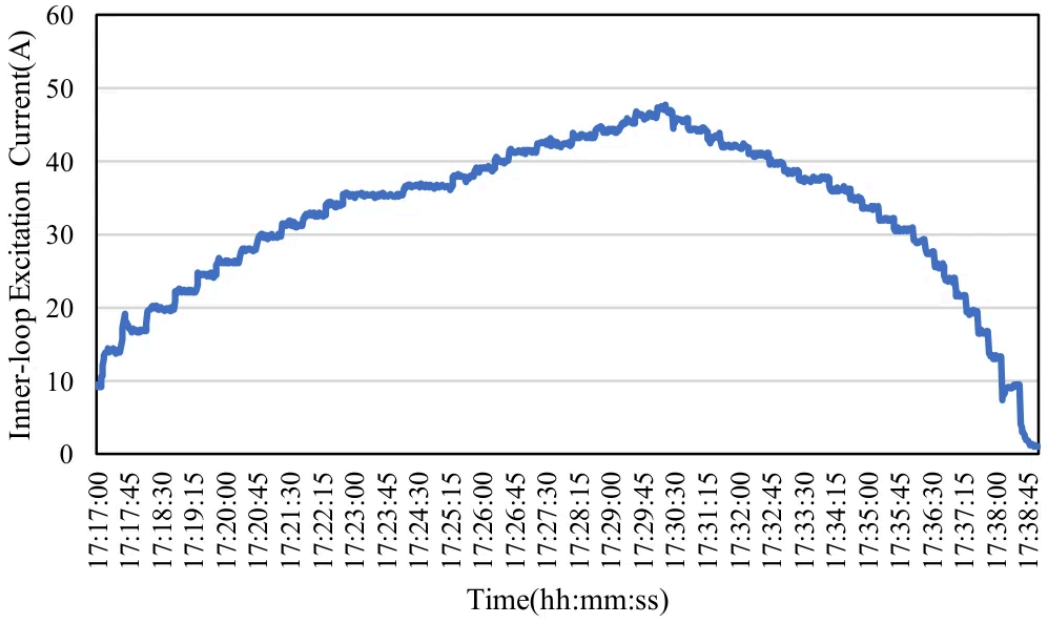


Figure 7. Inner-loop excitation current output waveform.

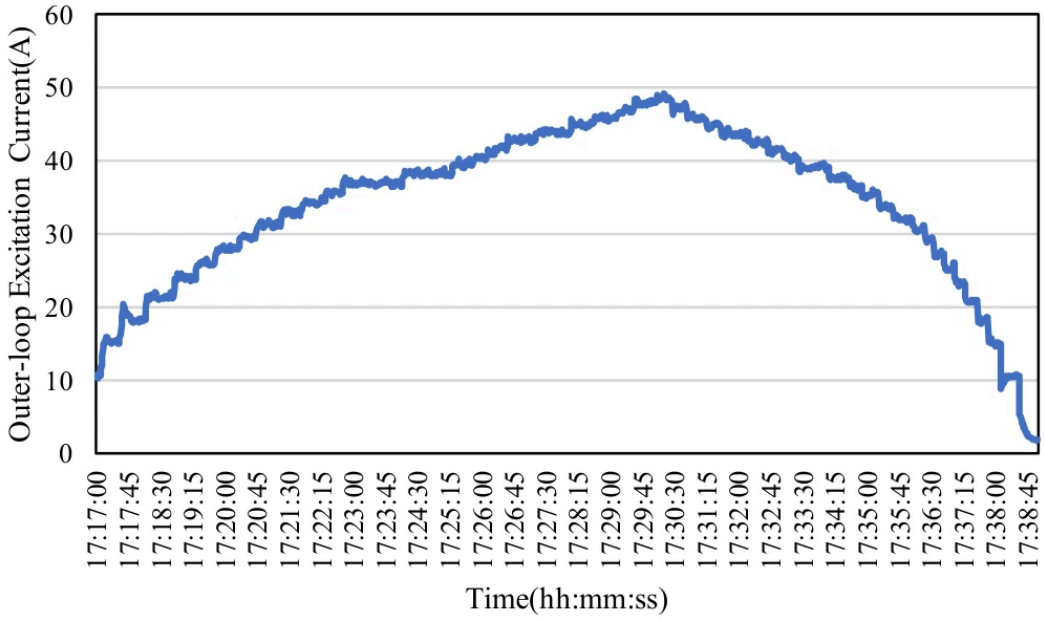


Figure 8. Outer-loop excitation current output waveform.

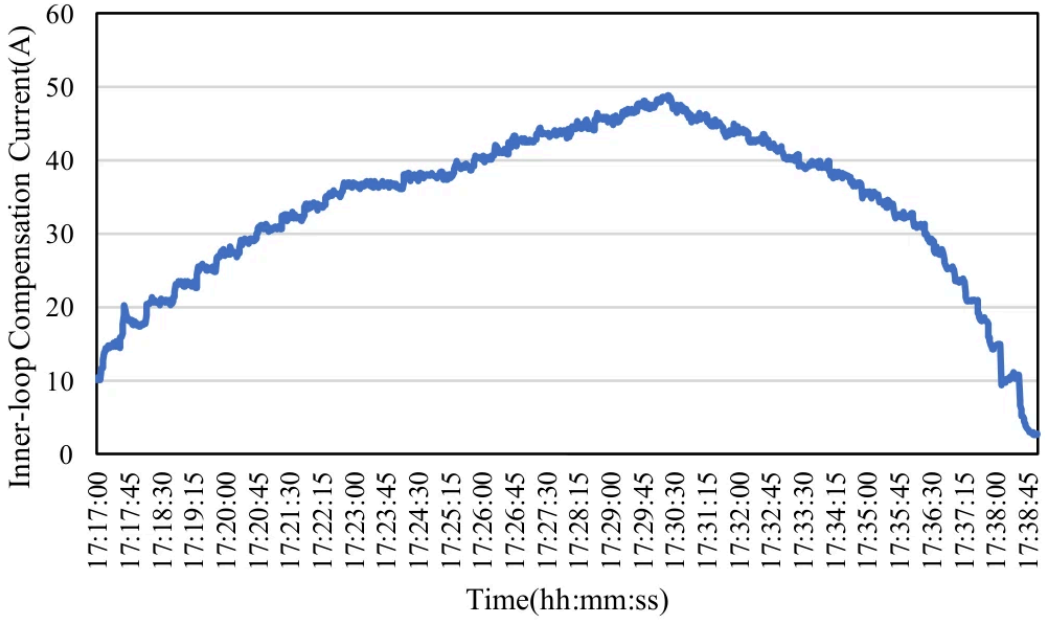


Figure 9. Inner-loop compensation current output waveform.

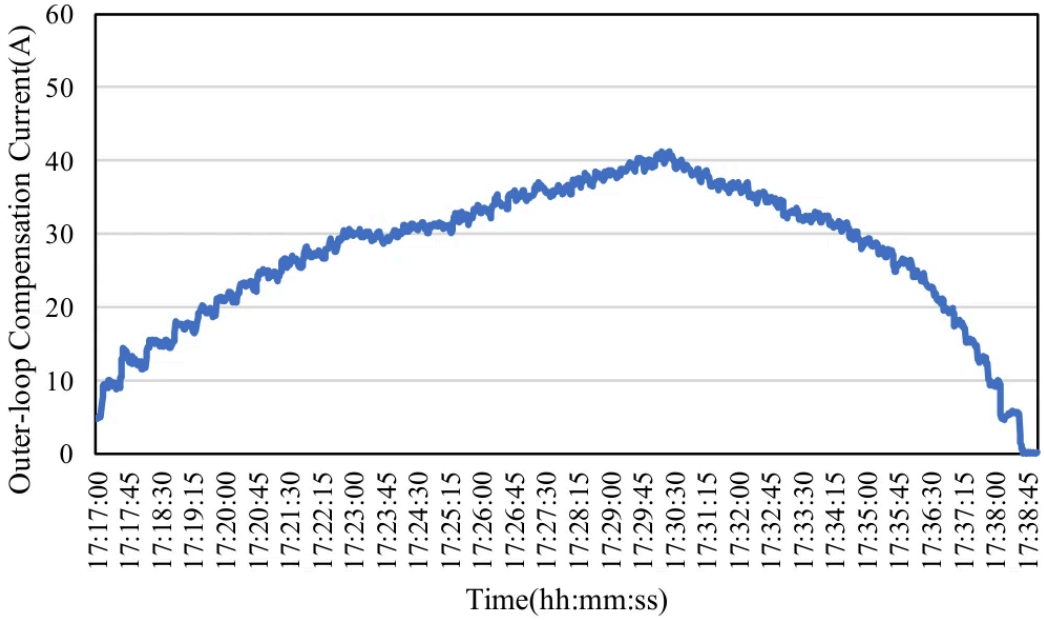


Figure 10. Outer-loop compensation current output waveform.

3.2. Main Shaft Swing and Air Gap Variation

Figures 11–13 show the X-direction and Y-direction main-shaft swing signals (measuring points 1 and 2) and the working air-gap length during the load-reduction process. During the whole test, the main shaft swing amplitude remains small. The working air gap instead varies within a band of about 0.5 mm around its 6 mm nominal value (approximately 8% of the nominal gap), decreasing slightly as the load-reduction ratio increases; this excursion is quasi-static, follows the load ramp, and does not indicate a loss of rotor position control. The coordinated control strategy introduces no additional vibration or rotor offset, which verifies the stability of the thrust balance control.

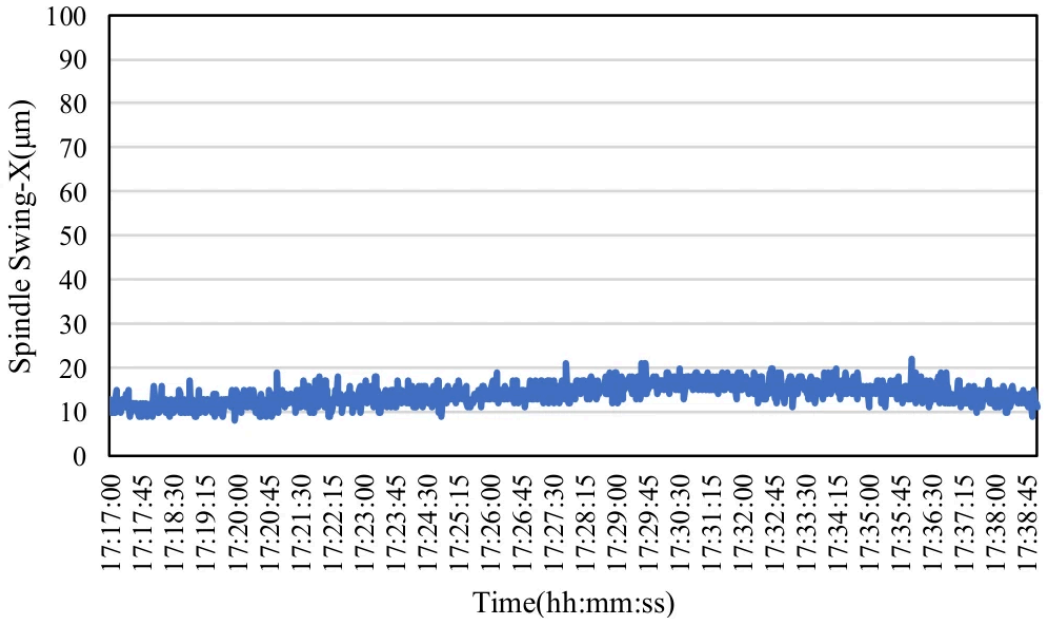


Figure 11. X-direction main-shaft swing waveform at measuring point 1.

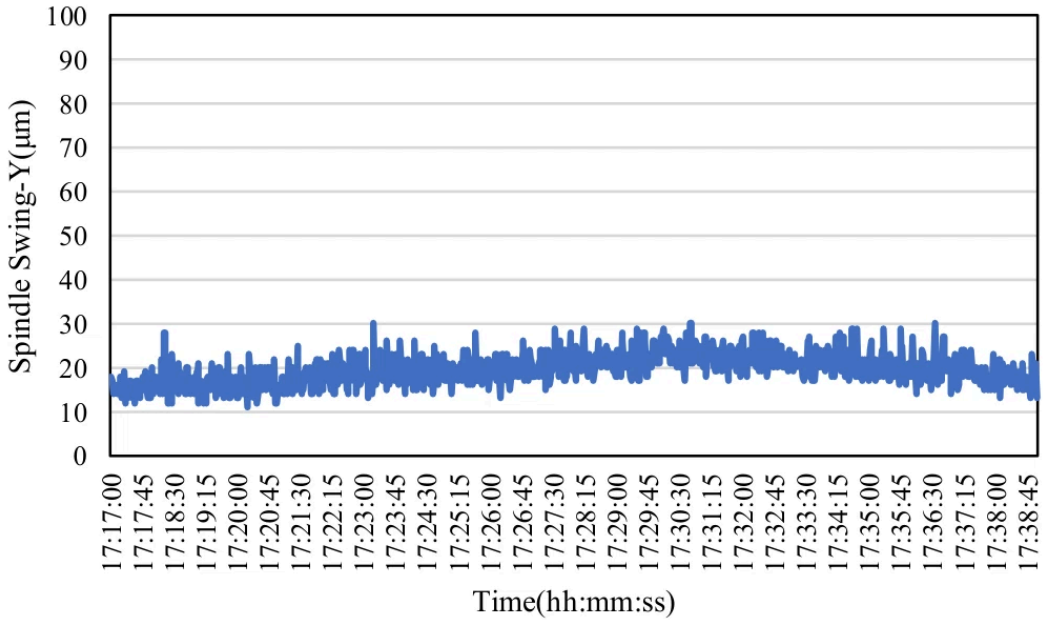


Figure 12. Y-direction main-shaft swing waveform at measuring point 2.

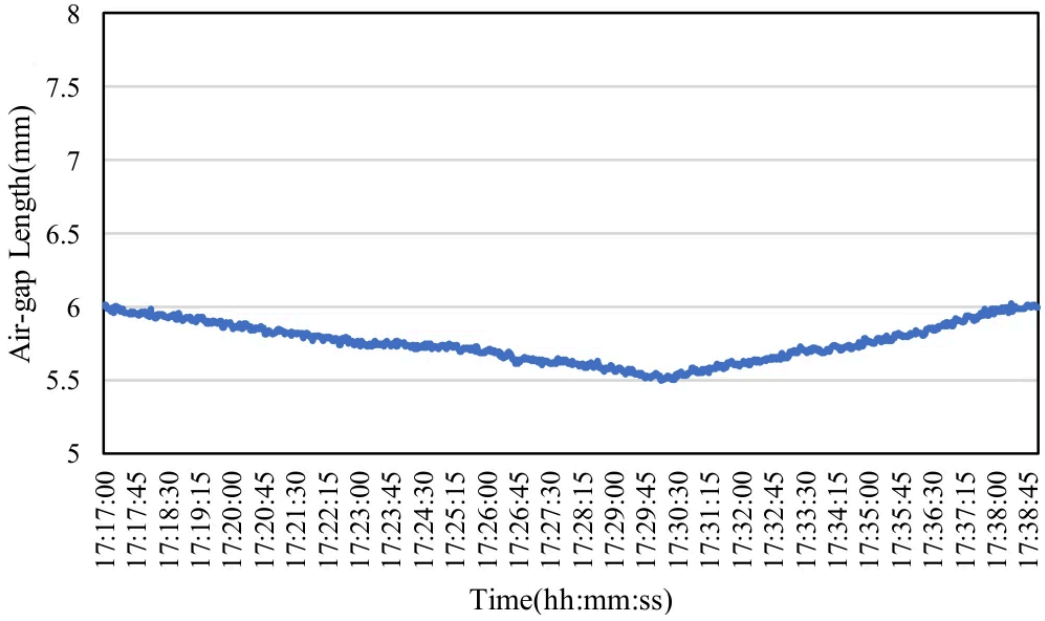


Figure 13. Working air-gap length waveform between the stator and rotating thrust disk.

The axial position of the rotor is determined by the balance between the total axial thrust (rotor weight plus hydraulic thrust) and the sum of two forces, namely the hydrodynamic oil-film force of the thrust bearing and the electromagnetic force of the actuator. Since the guide pads provide no axial positioning, the nominal 6 mm gap is not enforced by the guide-bearing system but is the equilibrium gap of this axial force balance. When the load-reduction ratio increases, part of the oil-film force is replaced by the electromagnetic force, so that the oil film becomes thinner and the rotor moves slightly toward the stator; together with the elastic deformation of the bearing housing and of the platform structure, this produces the air-gap excursion of about 0.5 mm seen in Figure 13. Because the excursion develops quasi-statically along the load ramp and is sensed by the capacitive displacement sensor that monitors the working air gap, the force loop uses the measured gap and flux signals to hold the electromagnetic force at its setpoint while the

gap varies. The electromagnetic actuator itself has a negative stiffness, since its attraction force grows as the gap decreases, and no active axial levitation loop is implemented on this platform, so the negative stiffness is not compensated electronically. Instead, the hydrodynamic oil film of the thrust bearing supplies the positive restoring stiffness; within the tested operating range this stiffness dominates the negative stiffness of the actuator, so that the combined axial stiffness stays positive and the equilibrium point remains stable, as evidenced by the bounded 0.5 mm excursion.

3.3. Flux Density and Flux Leakage Suppression Effect

Figures 14–18 show the main-pole flux density waveform and the inner-loop and outer-loop external leakage-flux density waveforms with compensation activated, together with the corresponding inner-loop and outer-loop waveforms without compensation (Figures 17 and 18). With the flux leakage compensation branches activated, the external leakage flux density is effectively suppressed, with a suppression rate exceeding 60% compared with the uncompensated condition, where the uncompensated condition is the same load-reduction ramp with both compensation branches disabled and the ratio is evaluated over the 20–80% load-reduction range. The compensation current adjusts automatically with the leakage flux, and no additional steady-state error is introduced. The main-pole flux density remains stable during the whole test, confirming that the flux leakage compensation does not disturb the main thrust control. The suppression rate is defined as the relative reduction in the external leakage-flux density after the compensation branches are enabled with respect to the uncompensated condition, evaluated at the inner-loop and outer-loop leakage-flux probes. Because the leakage field and the compensation field are axisymmetric, each probe reading is representative of the annular leakage path at its radius, i.e., on the bore side for the inner-loop probe and on the outer-diameter side for the outer-loop probe; the reported suppression therefore applies to the external leakage flux on these two sides of the actuator, and point-wise nulling of the stray field over the whole surrounding space is not claimed.

To make the comparison between the compensated and the uncompensated condition explicit, the two states are paired quantity by quantity in Table 3. Both records belong to the same test cycle, the same load-reduction ramp, the same rotational speed of 500 r/min and the same oil supply and inlet temperature, and the only variable between them is the enabling of the two compensation branches; the uncompensated record is therefore an ablation of the proposed scheme on one and the same hardware, and not a comparison between different machines or different operating conditions. This removes the operating-condition drift that would otherwise contaminate a before-and-after comparison: the rotor position, the oil-film state, the flux-density level and the sensor positions are identical in the two records, so the difference between them can be attributed to the compensation field alone.

Table 3. Comparison between the compensated and the uncompensated condition for the external leakage-flux density.

Probe and Quantity	Compensation Disabled (Reference)	Compensation Enabled	Suppression Ratio
Inner-loop external leakage-flux density, bore-side probe	Figure 17	Figure 15	≥60%
Outer-loop external leakage-flux density, outer-diameter probe	Figure 18	Figure 16	≥60%

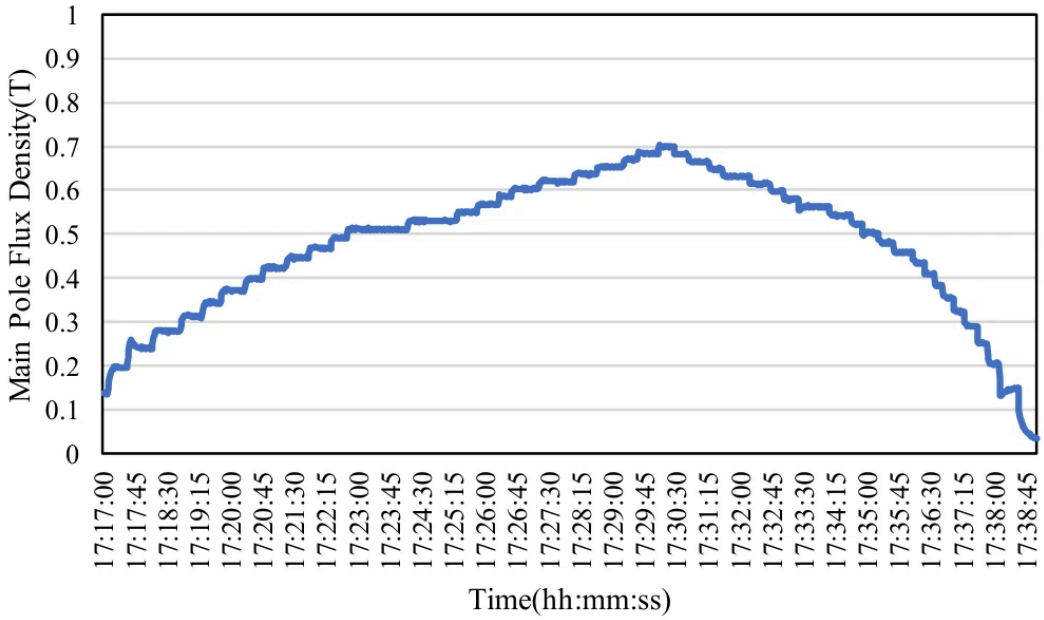


Figure 14. Main-pole flux density waveform (measuring point 3).

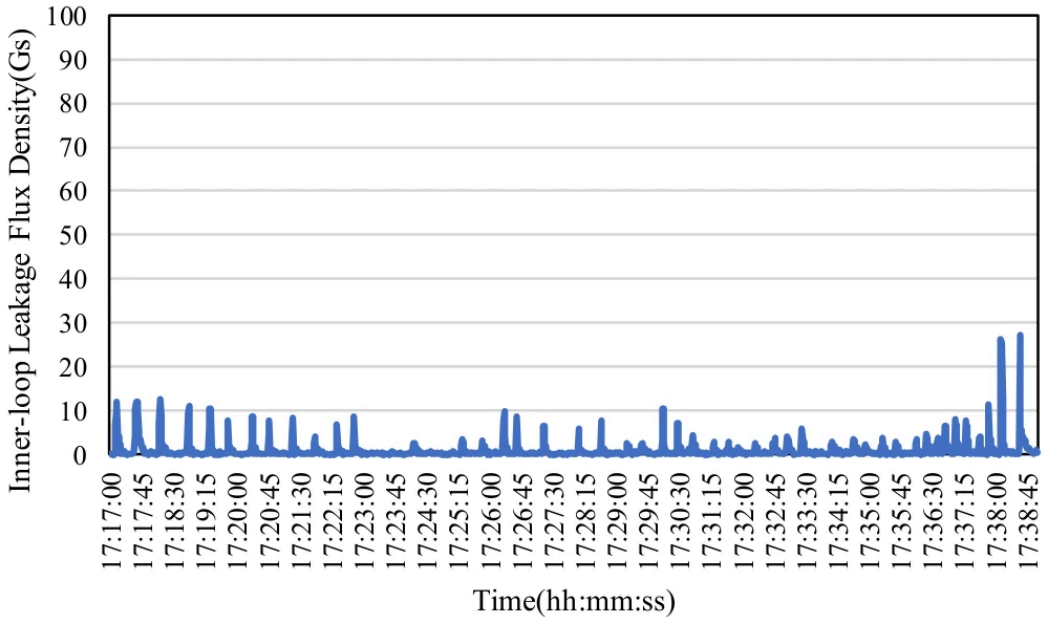


Figure 15. Inner-loop leakage-flux density waveform.

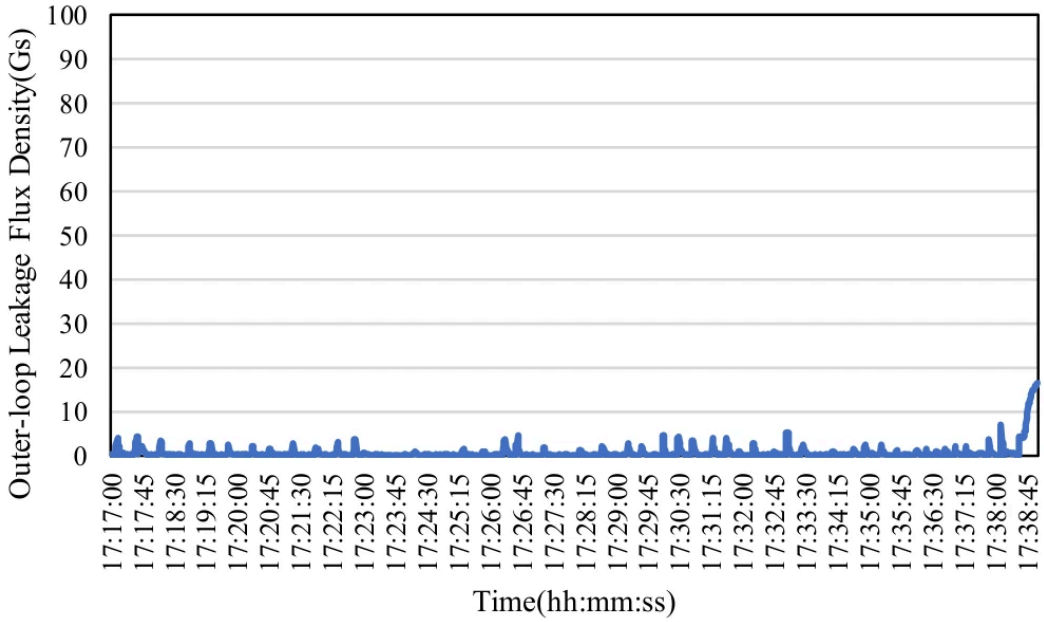


Figure 16. Outer-loop leakage-flux density waveform.

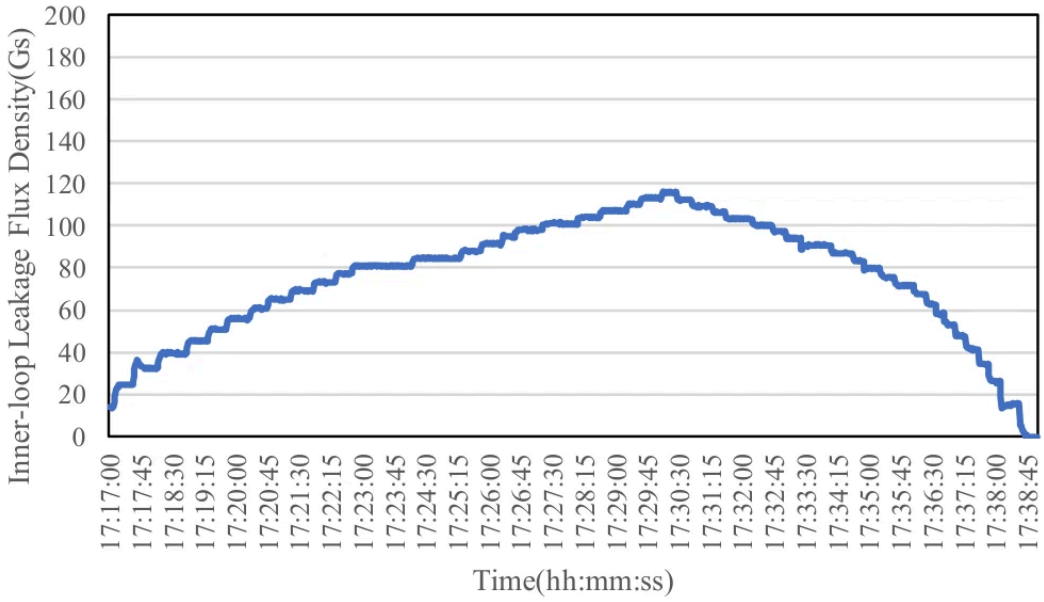


Figure 17. Inner-loop leakage-flux density waveform without flux-leakage compensation (uncompensated baseline).

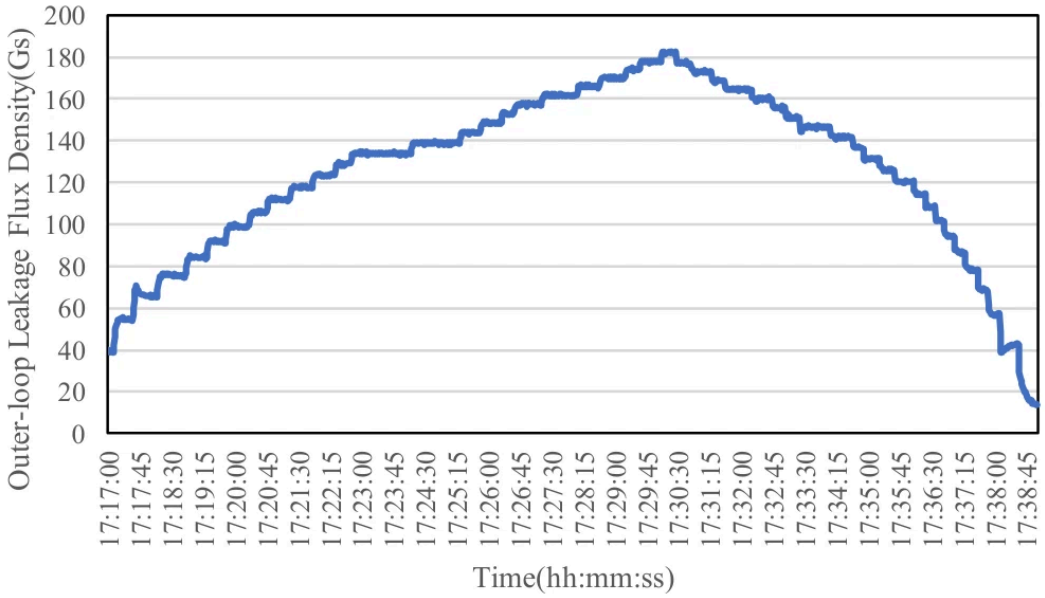


Figure 18. Outer-loop leakage-flux density waveform without flux-leakage compensation (uncompensated baseline).

The suppression ratio is evaluated at the steady-state points of the 20–80% load-reduction range as $\eta = 1 - B_comp/B_unc$, where B_unc is the leakage-flux density read at the same probe with both compensation branches disabled and B_comp is the value at the same probe with the branches enabled, both taken within the stabilized window of the same operating point. The ratio never falls below 60% on either the inner or the outer probe over the whole evaluated range, and the decrease of the leakage-flux density visible in Figures 15 and 16 with respect to the baselines of Figures 17 and 18 follows the compensation current of Figures 9 and 10, which confirms that the reduction is produced by the compensation field rather than by an incidental change of the operating point.

3.4. Oil-Film Thickness and Oil-Cavity Pressure

Figures 19 and 20 show the oil-film thickness measured by the eddy-current sensor and the oil-cavity pressure waveforms. As the thrust load on the bearing decreases, the oil-film thickness increases gradually, which is consistent with the theoretical analysis. During the transient load changes, the oil-film thickness remains stable without rapid fluctuation. The oil-cavity pressure follows the bearing load along the load-reduction ramp, anti-correlated with the reduced load weight of Figure 6 and the oil-film thickness of Figure 19: it decreases from about 5.3 MPa at the initial high-load condition to about 1.5 MPa at the maximum load-reduction ratio, and returns toward the initial level as the load is restored. This trend follows the mechanical load carried by the hydrodynamic film: as the electromagnetic actuator removes an increasing share of the rotor weight, the specific load on the bearing decreases, the oil film thickens, and the hydrodynamic pressure required to support the remaining load falls correspondingly; during reloading the film thins and the pressure recovers. The pressure therefore tracks the load-reduction ratio quasi-statically, and no abrupt pressure drop or surge is observed under the tested conditions. Under the complete coordinated control framework, these measured signals remain within the observed normal range; the present experiments do not isolate the independent contribution of the auxiliary feedforward or branch-coordination functions. For this bearing, the minimum safe threshold for oil-film thickness is 30 μm; the measured oil-film thickness stays above this threshold without rapid thinning under the

tested load-reduction conditions. This 30 μm value is an empirical safety criterion for the bearing hardware, not a threshold derived from sensor-calibration data, and the comparison is interpreted with the declared measurement accuracy of the eddy-current sensors in view.

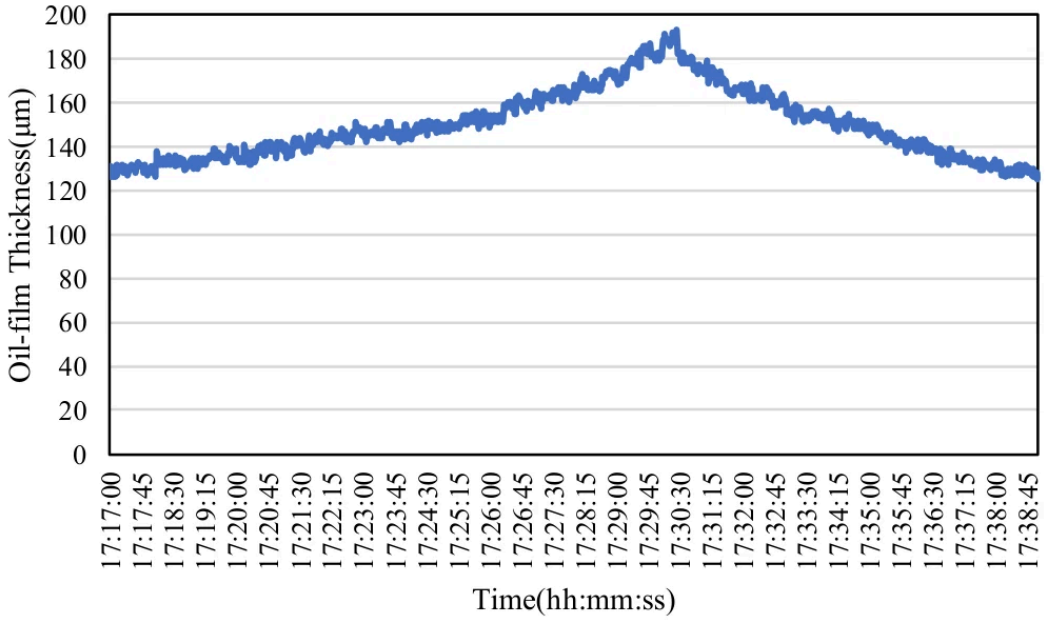


Figure 19. Oil-film thickness waveform.

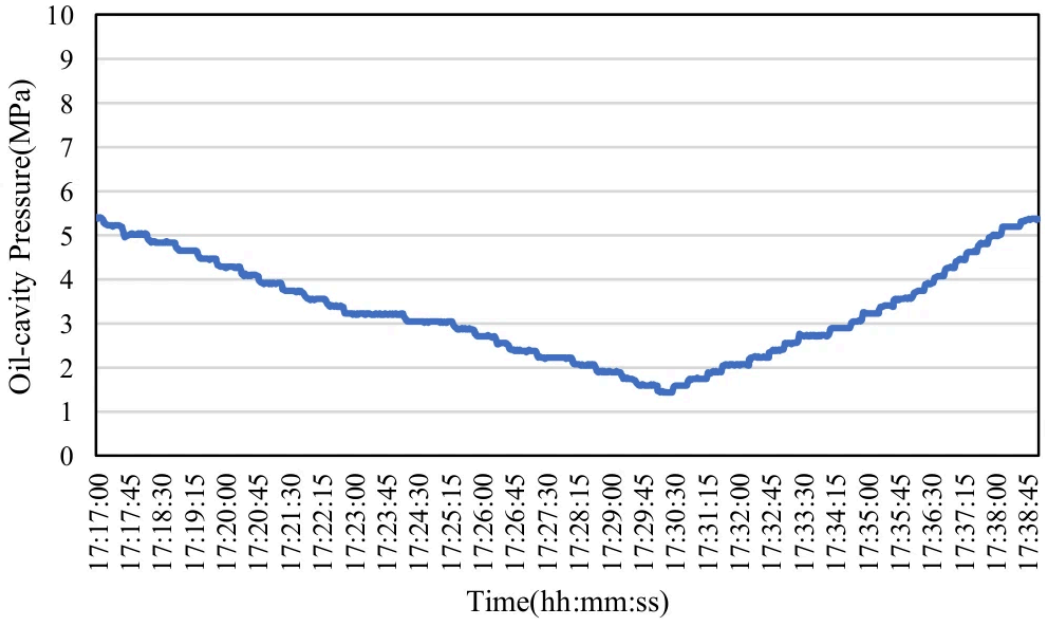


Figure 20. Oil-cavity pressure waveform.

3.5. Pad Temperature

Figures 21–25 show the temperature waveforms of the thrust pad, oil-film, coils, guide pad and loading pad during the continuous load-reduction operation. Each measured temperature remains stable and far below the defined temperature limits of the babbitt-lined thrust-pad bearing: 70 °C is the long-term design operating upper limit (warning level) under the load-reduced operating regime, and 75 °C is the protection intervention alarm threshold, above which the lubricant viscosity degrades markedly and

the oil-film failure risk rises; this 75 °C value is not the babbitt melting point, which is far higher. As the electromagnetic load-reduction ratio increases, the thermal load on the thrust bearing decreases correspondingly, and the temperature rise of the bearing pads is further suppressed. The temperature results verify that the electromagnetic load-reduction system effectively reduces the thermal stress of the thrust bearing under heavy-load conditions.

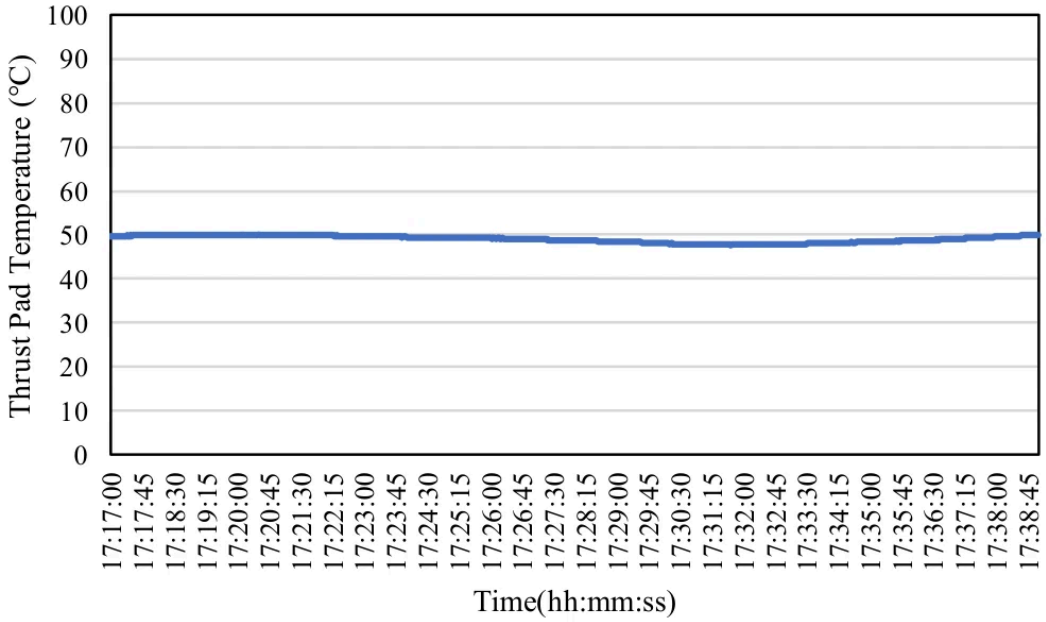


Figure 21. Thrust pad temperature waveform.

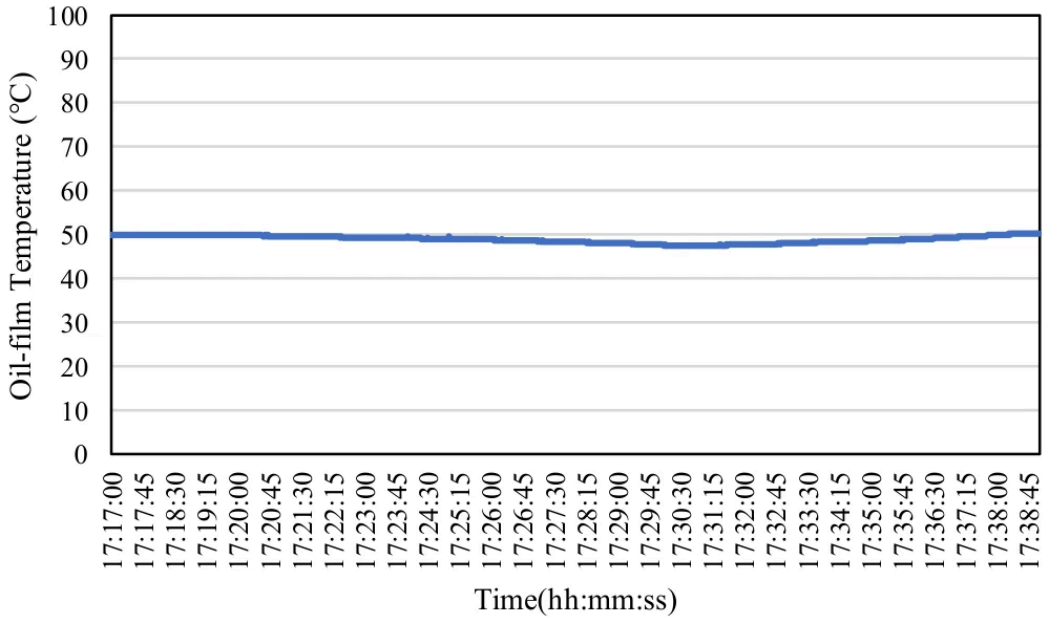


Figure 22. Oil-film temperature waveform.

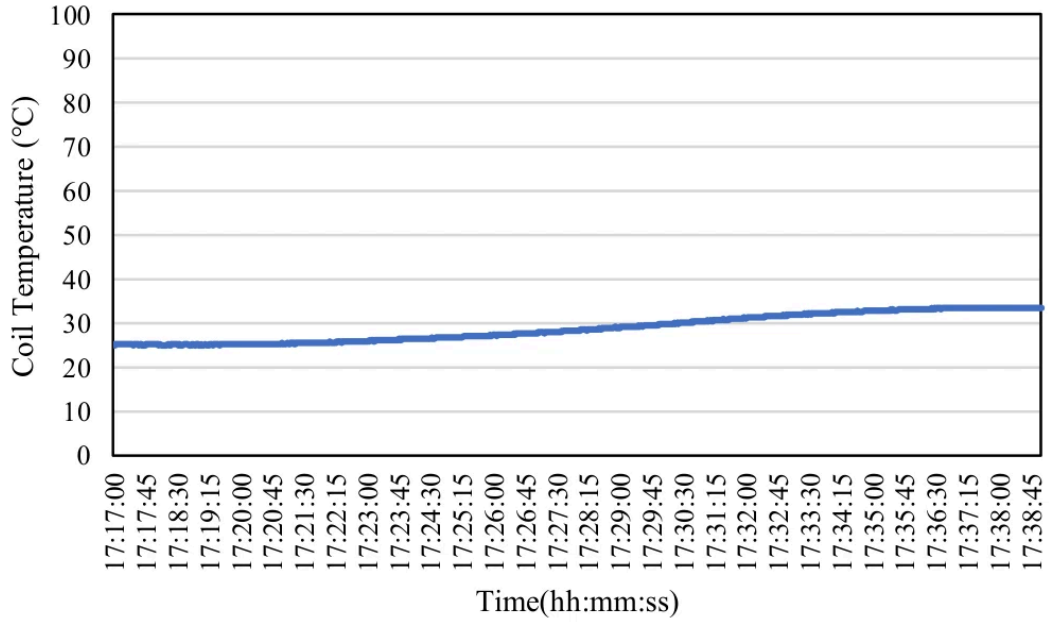


Figure 23. Coil temperature waveform.

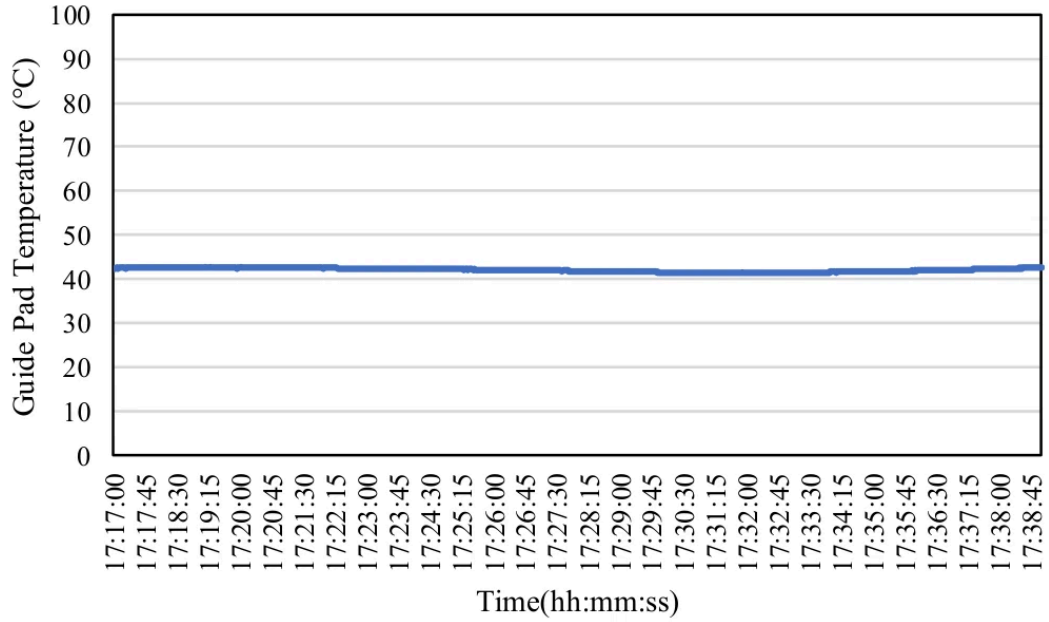


Figure 24. Guide pad temperature waveform.

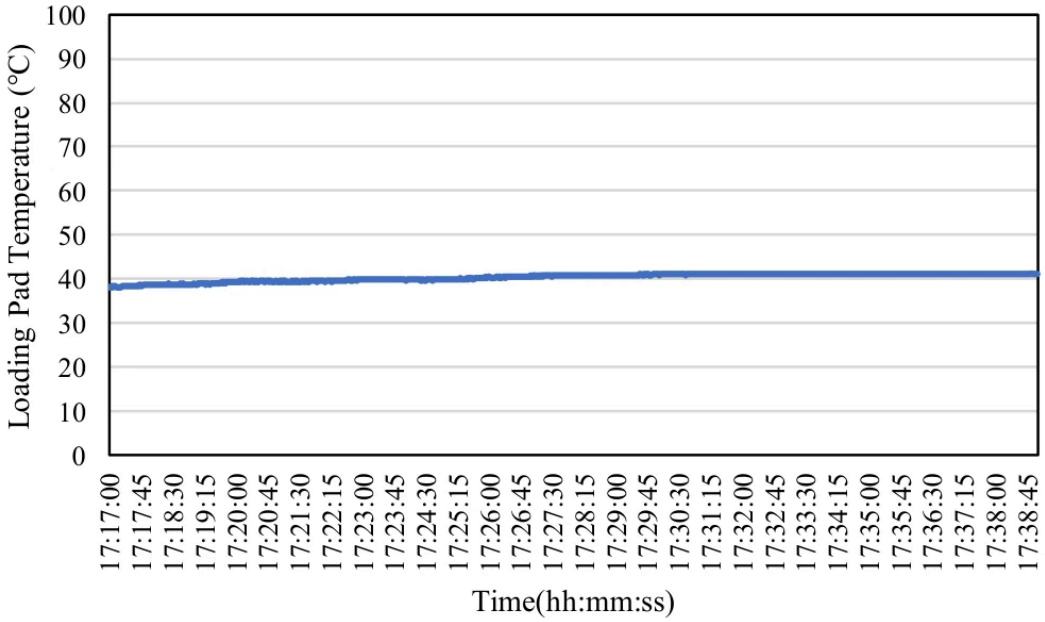


Figure 25. Loading pad temperature waveform.

3.6. Driving-Motor Current and Friction Reduction

The thrust bearing is the main source of the mechanical resistance overcome by the drive motor, so the stator current of the drive motor gives an indirect indication of the bearing friction loss. The stator current was recorded both in the steady-state cases, at load-reduction ratios of 0%, 20%, 40%, 60% and 80%, and continuously along the loading and load-reduction ramps, at a constant rotational speed of 500 r/min.

As the electromagnetic load-reduction force increases, the residual axial load carried by the thrust pads decreases and the hydrodynamic film becomes thicker, so the frictional resistance of the pads falls; the stator current of the drive motor therefore decreases as the load-reduction ratio increases, and recovers when the reduced load is removed, as shown in Figure 26. Since the rotational speed, the oil supply and the immersion depth of the runner are kept unchanged, the components of the current that do not depend on the bearing load, namely the oil churning loss, the guide-bearing friction and the intrinsic losses of the motor, remain essentially constant. The variation of the stator current is therefore attributed to the change of the thrust-pad friction loss, and the downward trend observed at increasing load-reduction ratio shows that electromagnetic load reduction lowers the friction of the thrust bearing.

This evidence is qualitative. The absolute value of the stator current cannot be converted into a friction power, because the load-independent components cannot be separated from the measurement and the efficiency of the drive train is not known. A quantitative friction-loss measurement with a torque transducer is therefore left to future work, as stated in Section 4.

3.7. Quantitative and Statistical Assessment

Beyond the descriptive waveforms, the experimental evidence is summarized in quantitative form in Table 4, which reports the value of each performance metric together with the condition under which it applies. The steady-state load-tracking error is defined as the relative deviation of the measured load-reduction weight from its setpoint in the stabilized segment, the leakage-suppression ratio is defined as the relative reduction of the external leakage-flux density with respect to the uncompensated baseline recorded on the same load-reduction ramp, and the air-gap excursion is expressed as the

deviation of the working air gap from its 6 mm nominal value. Over the 20–80% load-reduction range the worst-case tracking error is 3%, the air-gap excursion remains within 0.5 mm, and the minimum leakage-suppression ratio is 60% on both the inner and the outer probes, so that the quantitative bounds in Table 4 replace the purely descriptive statements of the waveform discussion.

Table 4. Summary of the quantitative performance metrics over the tested load-reduction range.

Metric	Reported Value	Condition
Steady-state load-tracking error	≤3%	20–80% load-reduction range (worst case)
Air-gap excursion	≤0.5 mm (≈8% of the 6 mm nominal gap)	quasi-static, follows the load ramp
Leakage-suppression ratio, inner probe	≥60%	compensation enabled vs. disabled, same ramp
Leakage-suppression ratio, outer probe	≥60%	compensation enabled vs. disabled, same ramp
Oil-film thickness	>30 μm	above the minimum safe threshold
Thrust-pad temperature	<70 °C	below the warning level (75 °C protection threshold)
Oil-cavity pressure	5.3 → 1.5 MPa	0% → maximum load-reduction ratio

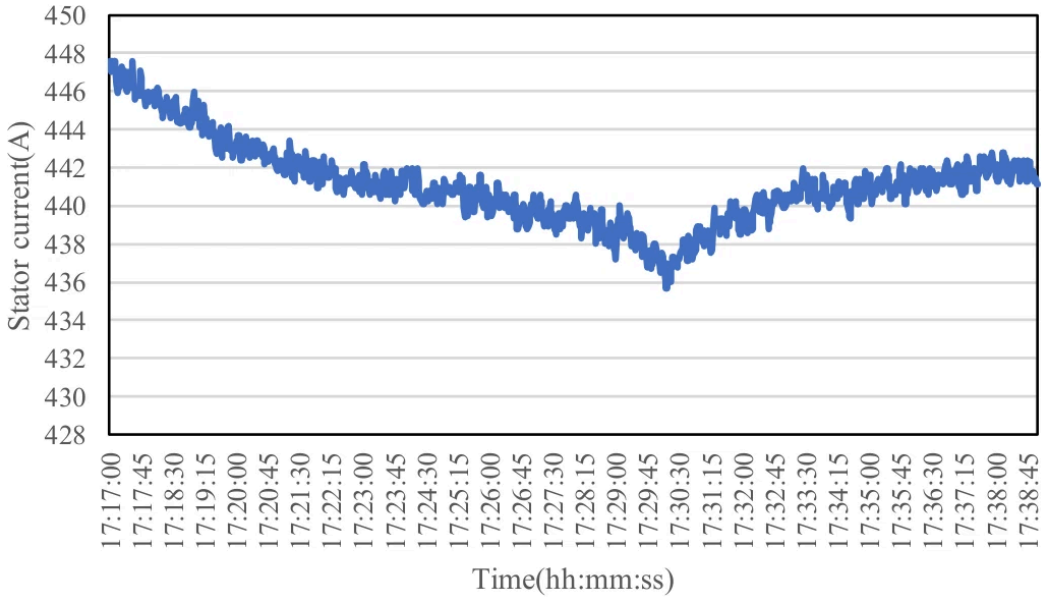


Figure 26. Stator current of the drive motor during the load-reduction ramp test: the current decreases as the load-reduction ratio increases and recovers when the reduced load is removed.

The signals are evaluated over a time window taken after all monitored quantities have stabilized, and both the mean value and the peak-to-peak span of the record within that window are reported, so that each quantitative statement is a bounded value rather than a single sample of the time series. This reporting protocol also bounds the influence of the sensor noise on the figures quoted in Table 4, since the declared accuracy of the displacement, flux-density, pressure and temperature sensors enters the peak-to-peak span of the corresponding record. The air-gap excursion quoted in Table 4 is obtained as the difference between the reading taken at a given load-reduction ratio and the reading taken at the 0% reference case, on the same measuring point and with the same capacitive channel; because both readings come from the same sensor, its zero offset and most of its gain error cancel in the difference, so that the quoted excursion is governed by the

short-term repeatability of that channel rather than by its absolute accuracy of ±3% FS, which corresponds to 0.36 mm over the 12 mm span and would otherwise be comparable with the excursion itself.

Regarding repeatability, each steady-state load-reduction ratio is reached twice within one test cycle, once along the loading path and once along the unloading path, and the two stabilized records are compared for each monitored quantity. The agreement between these two records provides the repeatability check of the steady-state values collected in Table 4, and the residual difference between them is retained within the peak-to-peak band stated above. A systematic multi-run repeatability campaign at each operating point, together with the quantitative friction-loss measurement mentioned in Section 3.6, is being prepared for the continuation of this work.

The controller parameters and the characteristics of the measurement channels on which the assessment relies are collected in Table 2, so that the settings used in the test campaign can be reproduced and the range of each channel can be read against the quantity it measures.

4. Discussion

Relative to the three gaps identified in the Introduction, the proposed scheme addresses single-loop control under magnetic-circuit nonlinearity, independent active leakage-flux compensation, and the need for heavy-duty experimental evidence. The experimental results validate the measured performance of the three-loop excitation main control and the independent leakage-flux compensation sub-module; multi-source sensing provides the measurement basis for these two controlled objectives. The nested load–magnetic-field–current three-loop architecture forms the core of the control strategy. The outer load loop ensures load-tracking precision; the intermediate magnetic-field loop overcomes the adverse effect caused by magnetic-circuit nonlinear saturation and hysteresis; the inner current loop provides fast disturbance suppression. Test results show that the steady-state load-regulation error remains lower than 3% within the 20–80% load-reduction interval under the tested operating conditions. The load and main-pole magnetic-field regulators combine pre-calibrated B–I/F–I lookup relations with recursive discrete-time PI regulation, while the excitation-current and compensation-current inner loops use conventional PI current regulators tuned experimentally; detailed transfer functions and tuning derivations are omitted because this work emphasizes the measured performance of the integrated platform. The controller parameters were tuned by trial-and-error on the 60 t-class platform and combined with the pre-calibrated B–I/F–I lookup relations; the steady-state error remains below 3% across the 20–80% load-reduction range and the response to step load changes is smooth, indicating robustness under the tested operating conditions. A systematic robustness analysis against large-magnitude plant-parameter variations has not been fully performed and is left for future work.

The oil-film-thickness feedforward channel and branch coordination functions are included as auxiliary implementation elements rather than separately validated contributions. In the present test campaign, the overall coordinated control maintained stable oil-film behavior, while the independent effect of these auxiliary functions was not isolated through comparative tests. For large-capacity thrust-bearing equipment, restraining short-time thrust fluctuation is critical to avoiding local oil-film rupture risk. The measured film thickness remains above the 30 μm safe lubrication threshold, but this overall observation should not be attributed to the auxiliary channel in isolation.

Based on stable main thrust regulation, the independent leakage-flux compensation sub-module further optimizes the overall system performance. Different from traditional passive magnetic-shielding methods, it adopts active reverse-magnetic-field counter-ac-

tion. An external leakage-flux suppression ratio of more than 60% is achieved, which improves the electromagnetic-force utilization efficiency and reduces electromagnetic interference to high-precision test sensors. The compensation branches operate without deteriorating the main load-regulation performance.

The inner and outer excitation and compensation branches operate in parallel under the overall control architecture. The present test campaign does not isolate the separate performance contribution of the output-coordination logic. Multi-point pad temperature data confirm the thermal-load reduction benefit brought by electromagnetic load reduction; all measured pad temperatures stay safely below the alarm threshold throughout the present test campaign.

The scope of the comparisons reported here should be stated explicitly. The comparison performed in this work is an ablation within one hardware configuration: the compensation branches are enabled and disabled along the same load-reduction ramp, and the leakage-flux density recorded with the branches disabled (Figures 17 and 18) is the reference against which the compensated waveforms (Figures 15 and 16) are compared; this isolates the contribution of the compensation sub-module. A controller-level comparison with a single current loop was not carried out on this platform, because bypassing the load and magnetic-field loops requires rewiring the signal chain and re-tuning the current regulator from scratch, i.e., a different controller and a separate commissioning campaign. The paper therefore does not claim a measured superiority over single-loop control; it quantifies, on the tested platform, the steady-state load-tracking accuracy, the leakage-flux suppression and the thermal benefit of the integrated architecture.

The present test is carried out on a 60 t-class platform, and future work will further verify the long-term operation stability and fault response characteristics of the control method under more complex operating conditions, such as sudden load-reduction system failure and speed fluctuation. A controlled comparison of the proposed cascade with a re-tuned single current loop on the same platform is the first item of this future work, so that the contribution of each loop can be quantified rather than inferred. In addition, the drive train will be equipped with a torque transducer, so that the friction loss of the thrust bearing can be measured directly under different operating conditions instead of being inferred from the stator current of the drive motor.

5. Conclusions

In this paper, a 60 t-class vertical electromagnetic load-reduction thrust-bearing test platform is constructed. The proposed control strategy consists mainly of multi-source signal acquisition, the load–magnetic-field–current three-loop excitation main control and the flux-leakage compensation sub-module; auxiliary oil-film signal processing and branch coordination functions were implemented but were not separately validated as independent contributions. Main conclusions are summarized as follows:

(1) The nested load–magnetic-field–current three-loop main control realizes high-precision steady-state load regulation. Within the load-reduction range of 20–80%, the steady-state regulation error is less than 3%.
(2) On the premise of guaranteeing the main thrust-regulation performance, the independent inner–outer flux-leakage compensation sub-module suppresses the external leakage flux by more than 60% over the 20–80% load-reduction range, with the same operating condition and compensation branches disabled as the reference, reduces electromagnetic interference and improves the electromagnetic-force utilization efficiency.
(3) Under the complete coordinated control framework, the measured oil-film thickness remains stable during the test and exceeds the minimum safe threshold of 30 μm;

this observation does not isolate the independent effect of the auxiliary feedforward or branch-coordination functions.

(4) Multi-point thrust-pad temperature test results show that electromagnetic load-reduction can effectively reduce the bearing thermal load; all pad-temperature measuring points remain below the alarm threshold under the test conditions; the two limits are defined in Section 3.5: 70 °C long-term design operating upper limit and 75 °C protection intervention threshold.

The proposed method provides an effective control solution for the engineering application of electromagnetic load-reduction technology in large vertical hydro-generator thrust bearings.

Author Contributions: Conceptualization, L.H. and J.B.; methodology, L.H.; validation, J.B.; formal analysis, L.H.; investigation, L.H. and J.B.; resources, J.B.; data curation, L.H. and J.B.; writing—original draft preparation, L.H.; writing—review and editing, J.B. and J.W.; visualization, L.H.; supervision, J.B. and J.W.; project administration, J.B. and J.W. All authors have read and agreed to the published version of the manuscript.

Funding: This research received no external funding.

Institutional Review Board Statement: Not applicable.

Informed Consent Statement: Not applicable.

Data Availability Statement: The experimental waveform data supporting the reported results are presented within the figures of this article. Raw time-series data are not publicly available due to project-related restrictions.

Acknowledgments: The authors thank Zhenbang Zhang and Pengyu Gao (Harbin Electric Machinery Company Limited) for their assistance in the test-platform commissioning, experimental data acquisition and preliminary processing of the measurement results. Their support is gratefully acknowledged.

Conflicts of Interest: Lijie Hu and Jing Bai were employed by the company Harbin Electric Machinery Company Limited. The remaining author declares that the research was conducted in the absence of any commercial or financial relationships that could be construed as a potential conflict of interest.

References

1. Jastrzebski, R.P.; Putkonen, A.; Zhuravlev, A.; Choudhury, T.; Sikanen, E.; Kurvinen, E.; Pyrhönen, J. Dynamics of a high-power AMB-multirotor drivetrain. *IEEE Trans. Ind. Electron.* **2024**, *71*, 9383–9393. [Google Scholar] [CrossRef]
2. Fan, L.; Liu, Z.; Wang, H.; Jiang, D.; Qu, R. Online vibration control for active magnetic bearing-based motor drive with improved gray wolf optimization. *IEEE Trans. Ind. Electron.* **2025**, *73*, 172–182. [Google Scholar] [CrossRef]
3. Bao, X.; Wang, X.; Han, B.; Ding, Q.; Zhang, Y. Eccentricity compensation for bearingless motor based on the tracking of the minimum antieccentric levitation current. *IEEE Trans. Ind. Electron.* **2024**, *71*, 3494–3503. [Google Scholar] [CrossRef]
4. Guan, B.; Wang, S.; Bao, X.-H. Thrust-bearing faults diagnosis using multiphase current signals with sub-Nyquist sampling. *IEEE/ASME Trans. Mechatron.* **2025**, *30*, 6085–6096. [Google Scholar] [CrossRef]
5. Wu, M.; Zhu, H.Q.; Zhang, H.; Zhang, W. Modeling and multilevel design optimization of an AC-DC three-degree-of-freedom hybrid magnetic bearing. *IEEE Trans. Ind. Electron.* **2022**, *69*, 10245–10254. [Google Scholar] [CrossRef]
6. Narsakka, J.; Madanzadeh, S.; Nerg, J.; Pyrhönen, J.; Sopanen, J. A multidisciplinary approach to the geometrical design of axial active magnetic bearings—Part I: Methodology. *IEEE Trans. Energy Convers.* **2026**, *41*, 211–221. [Google Scholar] [CrossRef]
7. Tang, P.X.; Li, G.L.; Li, Z.M.; Chen, Q.H. Thermally induced dynamics of an aero-engine active magnetic bearing-rotor system. *IEEE Trans. Magn.* **2026**, *62*, 7400210. [Google Scholar]
8. Zhang, T.; Le, Q.; Zhu, W. Structure and suspension force analysis of six-pole five-degrees-of-freedom AC hybrid magnetic bearing. *IEEE Trans. Magn.* **2021**, *57*, 8001404. [Google Scholar] [CrossRef]

9. Le, Y.; Sun, J.; Han, B. Modeling and design of a 3-DOF magnetic bearing for high-speed motor including eddy-current effects and leakage effects. *IEEE Trans. Ind. Electron.* **2016**, *63*, 3656–3665. [Google Scholar] [CrossRef]
10. Peng, C.; Sun, J.; Miao, C.; Fang, J. A novel cross-feedback notch filter for synchronous-vibration suppression of an MSFW with significant gyroscopic effects. *IEEE Trans. Ind. Electron.* **2017**, *64*, 7181–7190. [Google Scholar] [CrossRef]
11. Liu, C.; Liu, G. Autobalancing control for MSCMG based on sliding-mode observer and adaptive compensation. *IEEE Trans. Ind. Electron.* **2016**, *63*, 4346–4356. [Google Scholar] [CrossRef]
12. Zheng, S.; Han, B.; Feng, R.; Jiang, Y. Vibration-suppression control for AMB-supported motor driveline system using synchronous rotating frame transformation. *IEEE Trans. Ind. Electron.* **2015**, *62*, 5700–5708. [Google Scholar] [CrossRef]
13. Jiang, K.; Zhu, C.; Chen, L. Unbalance compensation by recursive seeking unbalance-mass position in active magnetic bearing-rotor system. *IEEE Trans. Ind. Electron.* **2015**, *62*, 5655–5664. [Google Scholar] [CrossRef]
14. Chen, Q.; Liu, G.; Han, B. Suppression of imbalance vibration in AMB-rotor systems using adaptive-frequency estimator. *IEEE Trans. Ind. Electron.* **2015**, *62*, 7696–7705. [Google Scholar] [CrossRef]
15. Yang, S.; Tsai, Y. Design of a thrust actuator for magnetic bearings with low radial attraction force. *IEEE Trans. Magn.* **2012**, *48*, 3587–3590. [Google Scholar] [CrossRef]
16. Sun, J.; Zhang, Y.; Liu, B.; Ge, X.; Zheng, Y.; Fernandez-Rodriguez, E. Research on oil mist leakage of bearing in hydropower station: A review. *Energies* **2022**, *15*, 2632. [Google Scholar] [CrossRef]
17. Ren, X.; Le, Y.; Sun, J.; Han, B. Magnetic-flux-leakage modeling and optimization of a combined radial-axial hybrid magnetic bearing. *IET Electr. Power Appl.* **2023**, *17*, 2112–2123. [Google Scholar]
18. Han, B.; Xu, Q.; Zheng, S. Integrated radial/thrust magnetic bearing without thrust disk for a high-speed driving system. *IET Electr. Power Appl.* **2016**, *10*, 276–283. [Google Scholar] [CrossRef]
19. Yu, Z.; Feng, W.; Sun, X.; Gu, Z.; Wen, C. 3D electromagnetic behaviors and discharge characteristics of superconducting flywheel energy storage system with radial-type high-temperature bearing. *IET Electr. Power Appl.* **2020**, *14*, 1865–1872. [Google Scholar] [CrossRef]
20. He, Y.; He, X.; Ma, J.; Fang, Y. Optimization research on a switching power amplifier and a current control strategy of active magnetic bearing. *IEEE Access* **2020**, *8*, 34833–34841. [Google Scholar] [CrossRef]

Disclaimer/Publisher's Note: The statements, opinions and data contained in all publications are solely those of the individual author(s) and contributor(s) and not of MDPI and/or the editor(s). MDPI and/or the editor(s) disclaim responsibility for any injury to people or property resulting from any ideas, methods, instructions or products referred to in the content.